

Monthly Weather Review
Physics-dynamics coupling with element-based high-order Galerkin methods: quasi equal-area physics grid
--Manuscript Draft--

Manuscript Number:	MWR-D-18-0136
Full Title:	Physics-dynamics coupling with element-based high-order Galerkin methods: quasi equal-area physics grid
Article Type:	Article
Corresponding Author:	Adam R. Herrington, M.S., 2011, University of Michigan State University of New York at Stony Brook Stony Brook, NY UNITED STATES
Corresponding Author's Institution:	State University of New York at Stony Brook
First Author:	Adam R. Herrington, M.S.
Order of Authors:	Adam R. Herrington, M.S. Peter H. Lauritzen, PhD Mark A. Taylor, PhD Steve Goldhaber, PhD Brian E. Eaton, PhD Julio T. Bacmeister, PhD Kevin A. Reed, PhD Paul A. Ullrich, PhD
Abstract:	Atmospheric modeling with element-based high-order Galerkin methods presents a unique challenge to the conventional physics-dynamics coupling paradigm, due to the highly irregular distribution of nodes within an element and the distinct numerical characteristics of the Galerkin method. The conventional coupling procedure is to evaluate the physical parameterizations ($\{\text{lem}\{\text{physics}\}\}$) on the dynamical core grid. Evaluating the physics at the nodal points exacerbates numerical noise from the Galerkin method, enabling and amplifying local extrema at element boundaries. Grid imprinting may be substantially reduced through the introduction of an entirely separate, approximately isotropic finite-volume grid for evaluating the physics forcing. Integration of the spectral basis over the control-volumes provides an area average state to the physics, which is more representative of the state in the vicinity of the nodal points rather than the nodal point itself, and is more consistent with the notion of a 'large-scale state' required by conventional physics packages. This study documents the implementation of a quasi-equal area physics grid into NCAR's Community Atmosphere Model with Spectral Elements, and is shown to be effective at mitigating grid imprinting in the solution. The physics grid is also appropriate for coupling to other components within the Community Earth System Model, since the coupler requires component fluxes to be defined on a finite-volume grid, and one can be certain that the fluxes on the physics grid are indeed, volume-averaged.



Click here to access/download

Cost Estimation and Agreement Worksheet
Journals_CEAW.pdf

Response to second round of revisions for “Physics-dynamics coupling with element-based high-order Galerkin methods: quasi equal-area physics grid”

In order to address a couple issues brought up by the reviewers, the aqua-planet simulations needed to be re-ran for additional analysis. The CAM4 physics package in the CESM2.1 code base is slightly modified from the original runs (most likely parameters in the Zhang-McFarlane deep convection scheme), and so the three aqua-planet plots look slightly different from the originals. The differences are minor and our conclusions are unchanged.

Reviewer 1

The revised version of the paper looks much better. I am glad to accept the paper with a minor change.

Line 364: For Andes "a lower latitudes" is within 10 to 20 degree from the equator but for Himalayas is within 20 to 30 degree.

The sentence has been modified at the reviewers request:

"At lower latitudes, over the Andes (between the equator and 20°S) or the Himalayas (from 20°N to 30°N), there is a clear preference for extrema to occur at the element boundaries (Figure 10)."

Line 365: their -> there

Fixed.

Figure 12 caption: ne30np3 -> ne30pg3

Fixed.

Reviewer 2

I want to thank the authors for taking the time to address all of my comments on the first draft of the manuscript. This new version of the article is well written and I think a valuable addition to the field. I would recommend it for publication.

I did have a few comments after reading the revised manuscript:

1) Lines 279 and 281, I think you mean se_nsplit instead of rsplit here. If I recall correctly, in CAM rsplit is substepped within the se_nsplit, which is substepped within the dt_physics. So the remap timestep is dt_physics / se_nsplit.

Yes, the reviewer is correct. The vertical remap is cycled nsplit times, and the text has been corrected.

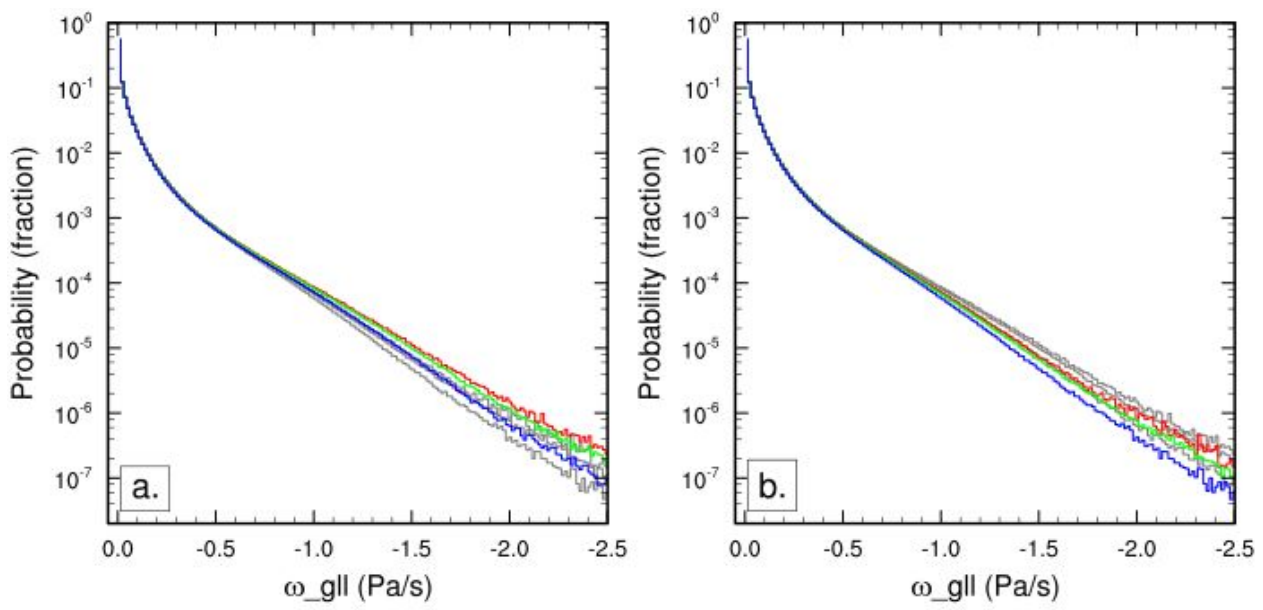
2) Figure 9, The authors state that the np4 and pg3 solutions look the same in this simulation, but looking at the plots on the left-hand side there are clearly some differences in features of the solution, especially at within 30 degrees of the equator. For example the temperature tendency for np4 near 180/25N has a strong negative patch that isn't present in the pg3 solution.

Similarly at around 100E/30S there are higher temp tendencies in the pg3 solution than the np4. Do the authors have an explanation for these differences? Could there be something having to do with the mapping of the tendencies from pg3 in physics to np4 in dynamics for the pg3 solution that is causing this? Are these related to topography, or another grid feature?

The reviewer is correct, that the pg3 simulation does not reach a peak mean low-level physics tendency like the one observed in the np4 simulation near 180/25N. The other peak the reviewer is referring to is a minimum; the red patch in the pg3 simulation near 100E/30S. We have added global means to the top of each plot in Figure 9, which effectively shows that the means and variances are slightly larger for np4 compared to pg3.

The plot suggests the physics tendencies may have larger magnitudes in np4 relative to pg3, albeit modestly. This is consistent with the mapping procedures in pg3. The tendencies are evaluated from the state on the pg3 grid, which are smoother due to integrating the basis functions over the pg3 control volumes. Therefore it follows that the tendencies, even before being mapped back to the GLL grid, are more damped relative the np4 runs. This effects the solution on the GLL grid, and drives the model accordingly.

An additional paragraph has been added to discuss the reviewers point (beginning at Line 347). That paragraph references a new version of Figure 3, and mentions that when plotting the pdf using the omega field on the GLL grid, in the pg3 run, the frequency of large magnitude omega is slightly lower, consistent with the reviewers observation. The plot of omega on GLL is provided for the reviewer:



Left is for the ne30np4 simulation, right is the ne30pg3 simulation. Colors are as in Figure 3a.

I thank the authors for their considered response to previous reviews. The majority of my previous points have been addressed, but I still have a few more comments. I am particularly keen that the last of these should be addressed.

- In my previous comment 4, I was suggesting clarification of ‘linear correlation preservation’ would be useful for the reader, not for my benefit! For readers that are not familiar with this, I still think it would be useful to say something on this after the list of requirements at line 249.

We have modified requirement 4 (line 202) to:

“linear correlation preservation, i.e., if field A is a linear function of B, this relationship is still preserved (see, e.g, equation 5 in Lauritzen and Thuburn 2012)”

- In figure 7, is there any need to include the plot of the constant field – surely it would suffice to say this in the text?

We have chosen to keep the second plot of the constant field, since it is illustrative of our point as a stand alone figure (if someone is just ‘browsing’ the manuscript).

- Regarding Figure 10 (previously Fig7), I don’t particularly find the circles beneficial. I would still rather see a difference plot (as you have done in Fig11) to make it easier to pick out and quantify the differences.

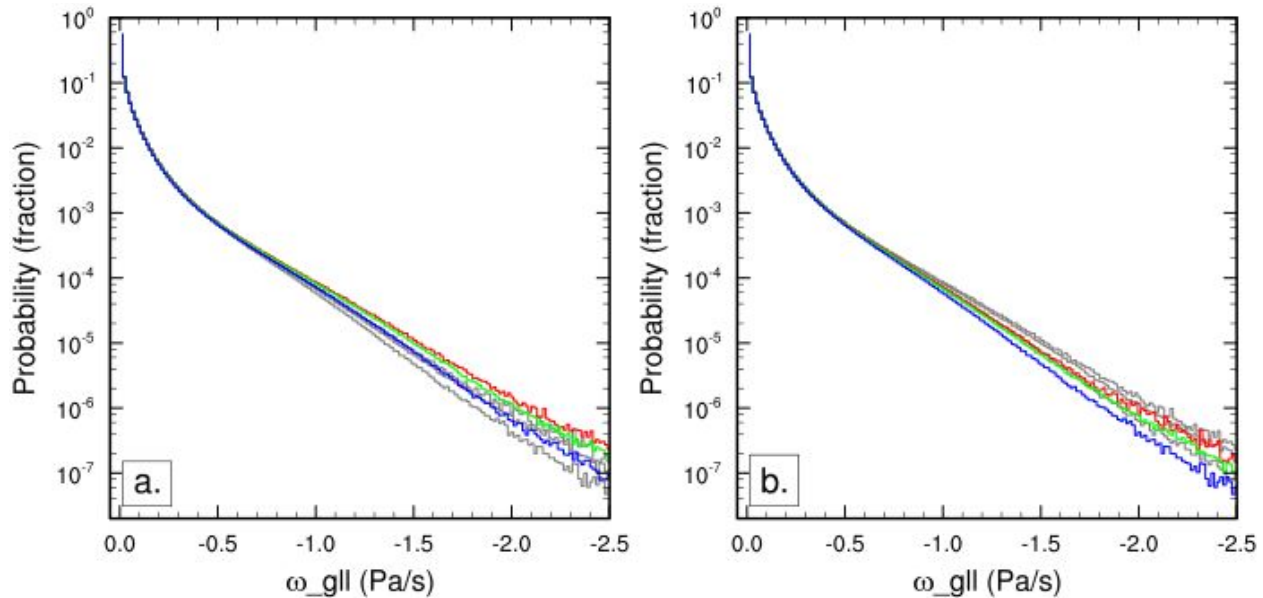
We have modified Figure 10 to have the same layout as Figure 11. The prior middle plot (the pg3 simulation on the GLL grid) was removed, and the difference plot was added, as the reviewer suggests. We thank the reviewer for being persistent on this point, since it nicely isolates grid imprinting in np4, and the improvement in grid imprinting in pg3. An additional line of text was necessary to explain the figure (Line 390).

- In my comment 7, I noted the change in the fractional values of large omega and suggested that overlaying the two plots would be helpful to see this. In your response you argue that this particular difference was due to the sampling differences and, having now changed the sampling method, the two figures are now more similar. While I agree, the curves have changed, I think there is still a significant difference that it would be good to highlight and could do with some explanation. See below for my poor man’s attempt at overlaying the curves – the gray curves in Fig 3a represent the data from Fig 3b and vice versa. I would like to see a plot like this and – if my quick attempt is not far from the truth – a comment on the fact that there seems to be a systematic increase in large omega values with the new method. (This is counter to my intuition which would lead me to expect systematically more frequent large omega values with the old anisotropic method).

We also thank the reviewer for his/her persistence on this point. The ‘poor man’s’ attempt is fairly close to the truth. It turns out, that this was an artifact of not using the exact same bin widths between all six curves - we let ncl determine the bin widths. This of course was not wise,

and we have re-done the figure using the same bin-widths (see new Figure 3). In addition, as the reviewer suggested, panel (a)'s curves are overlaid on panel (b) in grey, and vice versa. The result is much more consistent with the reviewers and our thinking - the larger magnitude vertical velocities are systematically less frequent in pg3.

An additional paragraph was added (beginning at Line 347) in response to another reviewers observation of Figure 9, that the mean and variance of the physics tendencies on the GLL grid are slightly lower in pg3 relative to np4. We therefore did another plot, like Flgure 3a that looks at the pdf of omega on the GLL grid, in the pg3 simulation. We do not show this in the text, but it is provided here for the reviewer:



Left is for the ne30np4 simulation, right is the ne30pg3 simulation. Colors and grey lines are as in Figure 3a.



Click here to access/download

Additional Material for Reviewer Reference

physgrid_markup.aux

1 **Physics-dynamics coupling with element-based high-order Galerkin**
2 **methods: quasi equal-area physics grid**

3 Adam R. Herrington*

4 *School of Marine and Atmospheric Sciences, Stony Brook University, Stony Brook, New York,*
5 *USA.*

6 Peter H. Lauritzen

7 *Climate and Global Dynamics, National Center for Atmospheric Research, 1850 Table Mesa*
8 *Drive, Boulder, Colorado, USA.*

9 Mark A. Taylor

10 *Sandia National Laboratories, Albuquerque, New Mexico, USA.*

11 Steve Goldhaber, Brian E. Eaton and Julio T. Bacmeister

12 *Climate and Global Dynamics, National Center for Atmospheric Research, 1850 Table Mesa*
13 *Drive, Boulder, Colorado, USA.*

14 Kevin A. Reed

15 *School of Marine and Atmospheric Sciences, Stony Brook University, State University of New*
16 *York, Stony Brook, New York.*

17 Paul A. Ullrich

¹⁸ Department of Land, Air and Water Resources, University of California, Davis, California, USA.

¹⁹ *Corresponding author address: Adam R. Herrington, School of Marine and Atmospheric Sciences, Stony Brook University, Stony Brook, New York, USA.

²⁰ E-mail: adam.herrington@stonybrook.edu

ABSTRACT

Atmospheric modeling with element-based high-order Galerkin methods presents a unique challenge to the conventional physics-dynamics coupling paradigm, due to the highly irregular distribution of nodes within an element and the distinct numerical characteristics of the Galerkin method. The conventional coupling procedure is to evaluate the physical parameterizations (*physics*) on the dynamical core grid. Evaluating the physics at the nodal points exacerbates numerical noise from the Galerkin method, enabling and amplifying local extrema at element boundaries. Grid imprinting may be substantially reduced through the introduction of an entirely separate, approximately isotropic finite-volume grid for evaluating the physics forcing. Integration of the spectral basis over the control-volumes provides an area average state to the physics, which is more representative of the state in the vicinity of the nodal points rather than the nodal point itself, and is more consistent with the notion of a ‘large-scale state’ required by conventional physics packages.

This study documents the implementation of a quasi-equal area physics grid into NCAR’s Community Atmosphere Model with Spectral Elements, and is shown to be effective at mitigating grid imprinting in the solution. The physics grid is also appropriate for coupling to other components within the Community Earth System Model, since the coupler requires component fluxes to be defined on a finite-volume grid, and one can be certain that the fluxes on the physics grid are indeed, volume-averaged.

43 **1. Introduction**

44 An increasing number of numerical methods publications in the atmospheric science literature
45 concern transport, shallow-water, and three-dimensional models employing element-based high-
46 order Galerkin discretizations such as finite-element and discontinuous Galerkin methods (for an
47 introduction to these methods see, e.g., Durran 2010; Nair et al. 2011; Ullrich 2014). Some global
48 models based on Galerkin methods have reached a level of maturity for which they are being con-
49 sidered for next generation climate and weather models due to their inherent conservation proper-
50 ties, high-order accuracy (for smooth problems), high parallel efficiency, high processor efficiency,
51 and geometric flexibility facilitating mesh-refinement applications. NCAR’s Community Atmo-
52 sphere Model (CAM; Neale et al. 2012) offers a dynamical core based on continuous Galerkin
53 finite elements (Taylor and Fournier 2010), referred to as CAM-SE (CAM Spectral Elements;
54 Taylor et al. 2008; Dennis et al. 2012; Lauritzen et al. 2018). CAM-SE is, in particular, being
55 used for high resolution climate modeling (e.g., Small et al. 2014; Reed et al. 2015; Bacmeister
56 et al. 2018) and static mesh-refinement applications (e.g., Fournier et al. 2004; Zarzycki et al.
57 2014a,b; Guba et al. 2014b; Rhoades et al. 2016). Other examples of models based on high-order
58 Galerkin methods that are being considered for ‘operational’ weather-climate applications are Gi-
59 raldo and Restelli (2008), Nair et al. (2009), Brdar et al. (2013) and the Energy Exascale Earth
60 System Model (<https://e3sm.org/>).

61 Assumptions inherent to the physical parameterizations (also referred to as *physics*) require
62 the state passed by the dynamical core represent a ‘large-scale state’, for example, in quasi-
63 equilibrium-type convection schemes (Arakawa and Schubert 1974; Plant and Craig 2008). In
64 finite-volume methods (e.g., Lin 2004), one may think of the dynamical core state as the average
65 state of the atmosphere over a control volume, and for resolutions typical of climate simulations

is entirely consistent with the notion of a ‘large-scale state’. For finite-difference methods (e.g., Suarez et al. 1983) the point value is thought of as representative for the atmospheric state in the vicinity of the point value and one can usually associate a volume with the grid-point. Hence the physics grid (the grid on which the state of the atmosphere is evaluated and passed to physics) and the dynamics grid (the grid the dynamical core uses) coincide. Having the physics and dynamics grids coincide is obviously convenient since no interpolation is needed (which could disrupt conservation properties) and the number of degrees of freedom on both grids is exactly the same.

For the regular latitude-longitude, cubed-sphere and icosahedral grids the distance between the grid-points is gradually varying for finite-volume/finite-difference discretizations. Examples of models that use these grids are CAM-FV (latitude-longitude grid, Lin 2004), FV3 (cubed-sphere grid, Putman and Lin 2007) and ICON (icosahedral grid, Wan et al. 2013). For high-order element-based Galerkin methods, the dynamical core grid is defined by the quadrature points. In CAM-SE, these are the Gauss-Lobatto-Legendre (GLL) quadrature nodes. A unique aspect of the high-order quadrature rules is that the nodes within an element are located at the roots of the basis set, which may be irregularly spaced. For example, Figure 1 shows GLL points on an individual element of a cubed-sphere grid for degree 3 ($np \times np = 4 \times 4$ quadrature points) and degree 7 ($np \times np = 8 \times 8$ quadrature points) Lagrange polynomial basis used in CAM-SE. The higher the order of the quadrature rule, the greater variance in distance between GLL quadrature points within an element. GLL quadrature points cluster near the edges and, in particular, the corners of the elements.

The resolved scales of motion are not determined by the distance between quadrature nodes, but rather the degree of the polynomial basis in each element. The nodes may be viewed as irregularly spaced samples of an underlying spectrally truncated state. From this perspective, one might expect the nodal solutions to be independent of location within an element. While the

90 interior quadrature nodes are C^∞ in CAM-SE (i.e. the basis representation is infinitely smooth
91 and all derivatives are continuous), the smoothness of boundary nodes are constrained by the
92 need to patch neighboring solutions together to form the global basis set, an operation known as
93 the direct stiffness summation (DSS; Maday and Patera 1987; Canuto et al. 2007). The DSS
94 operation is attractive because it allows for high-order accuracy with minimal communication
95 between elements, but degrades the solution to C^0 at element boundaries (i.e., all derivatives are
96 discontinuous). Through evaluating the physics at the nodal points, strong grid-scale forcing or
97 oscillatory behavior near an element boundary may exacerbate the discontinuity, and our initial
98 expectation, that the nodal solutions are independent of within-element location, is unlikely for
99 non-smooth problems, e.g., the presence of rough topography or moist physics grid-scale forcing.

100 It is the purpose of this paper to document the implementation of an entirely separate, quasi-
101 equal area finite-volume physics grid into CAM-SE. The use of a separate physics grid is not
102 entirely unheard of; prior studies have utilized the infrastructure developed for global-spectral
103 transform methods to experiment with different physics grids (Williamson 1999; Wedi 2014). In
104 our framework, the dynamical core state is integrated over control volumes to provide a volume av-
105 eraged state to the physics, thereby minimizing the influence of any one particular nodal value on
106 the physics forcing. Section 2 provides a thorough explanation of how grid imprinting manifests
107 in high-order Galerkin methods for non-smooth problems. The implementation of the physics grid
108 configuration into CAM-SE is presented in Section 3. Results from a hierarchy of idealized model
109 configurations are presented in Section 4, illustrating the physics grid is effective at mitigating un-
110 desirable grid imprinting in the solution. Section 5 contains a discussion of results and concluding
111 remarks.

¹¹² **2. The Quadrature Node Problem**

¹¹³ Figure 2 is a schematic illustrating in one-dimension how grid-imprinting is enabled by the
¹¹⁴ physics, when the dynamical core is built using high-order Galerkin methods. The schematic
¹¹⁵ depicts a time-step, starting from smooth initial conditions (Figure 2a), and subsequently advanc-
¹¹⁶ ing the dynamics one Runge-Kutta time-step (Figure 2b). Since the boundary nodes of adjacent
¹¹⁷ elements overlap one-another, there are now two solutions for each boundary node. The DSS op-
¹¹⁸ erator, effectively a numerical flux applied to the element boundaries such that overlapping nodal
¹¹⁹ values agree, is applied (Figure 2c), rendering the solutions at element boundaries C^0 ; less-smooth
¹²⁰ than neighboring C^∞ interior nodes. An element boundary discontinuity may be exacerbated if,
¹²¹ e.g., the physics updates the state at an element boundary (Figure 2d,e), resulting in characteristi-
¹²² cally tighter gradients on the boundary nodes compared to if the physics forcing were applied to
¹²³ an interior node (Figure 2g,h).

¹²⁴ To test the degree to which nodal solutions depend on within-element position, an aqua-planet
¹²⁵ simulation (Neale and Hoskins 2000; Medeiros et al. 2016), which consists of an ocean covered
¹²⁶ planet in perpetual equinox, with fixed, zonally symmetric sea surface temperatures idealized after
¹²⁷ the present day climatology, is carried out using CAM-SE, using CAM, version 4 physics (CAM4;
¹²⁸ Neale et al. 2010) and run for one year. The nominal low resolution *ne30np4* grid is used, pertain-
¹²⁹ ing to an average equatorial grid spacing of 111.2km. The probability density distribution of the
¹³⁰ upward vertical pressure velocity (ω), conditionally sampled based on three categories - ‘interior’,
¹³¹ ‘edge’ and ‘corner’ nodes - is provided in Figure 3a. The motivation for assessing noise in the ω
¹³² field comes from its connection with the atmosphere’s divergent modes, as follows from the con-
¹³³ tinuity equation in pressure coordinates. These modes are in turn sensitive to the within-element
¹³⁴ inhomogeneity of the pressure gradient that emerges from high-order Galerkin methods. There is

135 an apparent dependence on nodal location, with interior nodes being characteristically sluggish,
136 and corner and edge nodes having systematically larger magnitude vertical motion. This behavior
137 is consistent with the smoothness properties of the different nodal locations, with discontinuous
138 pressure gradients resulting in greater vertical motion at edge and corner nodes. The main division
139 of solutions shown in Figure 3a is primarily between whether a node is, or is not situated on an
140 element boundary, and is a nuanced signature of high-order element-based Galerkin methods for
141 non-smooth problems.

142 If the conventional physics-dynamics coupling paradigm is applied to CAM-SE, then the physics
143 are to be evaluated at the GLL nodes, and a volume associated with the quadrature point should
144 be defined. One approach to construct this grid is to decompose each spectral element into
145 $(np - 1) \times (np - 1)$ subcells and then take the dual grid of this subcell grid. For cubed-sphere
146 meshes, this dual grid will have a control volume associated with each quadrature point. These
147 control volumes will be triangles for the cube corner quadrature points and quadrilaterals for all
148 remaining quadrature points. Newton iteration can than be used to adjust the corners of these
149 control volumes so that their spherical area exactly match the Gaussian weight multiplied by the
150 metric term (these weights are used for integrating the basis functions over the elements and can
151 therefore, in this context, be interpreted as areas). For cubed-sphere meshes, the Newton itera-
152 tion can be replaced by a direct method if some of the quadrilaterals are replaced by pentagons
153 giving additional flexibility in matching the spherical area to the quadrature weights. Such a dual
154 grid is shown in Figure 4. This grid is used in the NCAR CESM (Community Earth System
155 Model) coupler for passing states between ocean, atmosphere and land components since the cur-
156 rent remapping method is finite-volume based and therefore requires control volumes (it is noted
157 that methods exist that do not require control volumes for conservative interpolation, e.g., Ullrich
158 and Taylor (2015)). Hence the components ‘see’ an irregular atmospheric grid. Similarly, the pa-

159 parameterizations in the atmosphere ‘see’ a state that is anisotropically sampled in space (see Figure
160 1 and 5 in Kim et al. 2008).

161 The quadrature grid in element-based Galerkin methods is defined to perform mathematical
162 operations on the basis functions, e.g., computing gradients and integrals, rather than evaluating
163 the state variables for physics-dynamics coupling. One may argue that it would be more consistent
164 to integrate the basis functions over quasi-equal area control volumes within each element and
165 pass those control volume average values to physics rather than irregularly spaced quadrature point
166 values. In this case when integrating basis functions over control volumes a grid-cell average value
167 is more representative of the values near the extrema at the element boundary than the quadrature
168 point value. The relationship between the nodal values, the basis functions and the proposed
169 control volumes is illustrated schematically in one-dimension in parts (f) and (i) in Figure 2.

170 3. Methods

171 Here we focus on CAM-SE, however, in principle the methods apply to any element-based high-
172 order Galerkin model. The physics grid in CAM-SE is defined by sub-dividing each element using
173 equi-angular gnomonic coordinate lines to define the sides of the physics grid control volumes (see
174 the Appendix for details). Note that the element boundaries are defined by equi-angular gnomonic
175 grid lines. The notation $pg = 3$ refers to the configuration where the elements are divided into
176 $pg \times pg = 3 \times 3$ equi-angular physics grid cells (see Figure 5) resulting in a quasi-equal spherical
177 area grid resembling the cubed-sphere. Defining the physics grid by sub-dividing elements makes
178 it possible to use the same element infrastructure as already used in CAM-SE, thereby facilitating
179 its implementation. Here we make use of the $ne30np4$ and $ne30pg3$ grids that use GLL quadrature
180 point physics grid (physics and dynamics grid coincide), and the same ($pg = 3$) resolution quasi

181 equal-area physics grids, respectively. In all configurations we use degree three Lagrange basis
182 ($np = 4$) and $ne \times ne = 30 \times 30$ elements on each cubed-sphere panel.

183 A consequence of separating physics and dynamics grids is that the atmospheric state must be
184 mapped to the physics grid and the physics tendencies must be mapped back to the dynamics
185 grid. This is discussed in separate sections below. When separating physics and dynamics grids it
186 is advantageous to use a vertical coordinate that is static during physics-dynamics coupling. This
187 was one motivation to switch to a dry-mass vertical coordinate in CAM-SE (Lauritzen et al. 2018);
188 since dry mass remains constant throughout physics the dry-mass vertical coordinate remains fixed
189 during physics-dynamics coupling. The dry mass coordinate subsequently evolves as floating
190 Lagrangian layers by the dynamics (Lin 2004) periodically mapped back to a reference hybrid-
191 sigma-pressure coordinate after Simmons and Burridge (1981). All variables mapped between
192 grids are collocated, layer-mean values (Lauritzen et al. 2018).

193 a. *Mapping state from dynamics grid (GLL) to physics grid (pg)*

194 The dynamics state is defined on the GLL grid in terms of temperature $T^{(gll)}$, zonal wind com-
195 ponent $u^{(gll)}$, meridional wind component $v^{(gll)}$, and dry pressure level thickness $\Delta p^{(gll)}$. In the
196 mapping of the atmospheric state to the physics grid it is important that the following properties
197 are met:

- 198 1. conservation of scalar quantities such as mass and dry thermal energy,
- 199 2. for tracers; shape-preservation (monotonicity), i.e., the mapping method must not introduce
200 new extrema in the interpolated field, in particular, negatives,
- 201 3. consistency, i.e., the mapping preserves a constant,

202 4. linear correlation preservation, i.e., if field A is a linear function of B , this relationship is still
 203 preserved (see, e.g, equation 5 in Lauritzen and Thuburn 2012)

204 Other properties that may be important, but not pursued here, includes total energy conservation
 205 and axial angular momentum conservation. Total energy is a quadratic quantity that is inherently
 206 difficult to conserve unless one maps total energy requiring one to diagnose either temperature or
 207 momentum components. For example, enforcing total energy conservation locally using, e.g., Lin
 208 (2004)'s method where total energy and velocity components are remapped and temperature is a
 209 derived variable, has proven problematic (C. Chen, personal communication). Similarly conserva-
 210 tion of axial angular momentum is problematic. Conservation of angular momentum requires one
 211 to interpolate the zonal and meridional components of momentum which creates large errors near
 212 the poles. To avoid the pole problem we interpolate contra-variant components of the momentum
 213 vector, which violates axial angular momentum conservation.

214 We argue that the most consistent method for mapping scalar state variables from the GLL grid
 215 to the physics grid is to integrate the Lagrange basis function representation (used by the SE dy-
 216 namical core) over the physics grid control volumes, i.e., integrate the basis function representation
 217 of $\Delta p^{(gll)} \times T^{(gll)}$ and $\Delta p^{(gll)}$ over the physics grid control volume (see, e.g., Lauritzen et al. 2017;
 218 Ullrich and Taylor 2015)

$$\Delta p^{(pg)} = \frac{1}{A^{(pg)}} \int_{A^{(pg)}} \Delta p^{(gll)} dA, \quad (1)$$

$$T^{(pg)} = \frac{1}{A^{(pg)} \Delta p^{(pg)}} \int_{A^{(pg)}} T^{(gll)} \Delta p^{(gll)} dA, \quad (2)$$

219 where $A^{(pg)}$ is the physics grid area. The integrals are numerically computed using the GLL
 220 quadrature rule on each physics grid element, which exactly (to machine precision) integrates the
 221 basis functions over the pg control volumes (Lauritzen et al. 2017). Thermal energy and dry air
 222 mass is conserved and the mapping is consistent. For the wind, which is a vector, the zonal and

223 meridional wind components are mapped by transforming to contra-variant wind components,
224 evaluating the basis function representation thereof at the equi-angular center of the physics grid
225 control volumes and then transformed back to latitude-longitude coordinate system winds. All of
226 the operations are local to the element and do not require communication between elements.

227 The mapping of tracers is more problematic since the SE basis function representation is oscil-
228 latory although the shape-preserving filter guarantees shape-preservation at the GLL nodes (Guba
229 et al. 2014a). To avoid this issue we use the CAM-SE-CSLAM version of CAM-SE (Conservative
230 Semi-Lagrangian Multi-tracer transport scheme Lauritzen et al. 2017), where tracers are advected
231 on the $pg = 3$ physics grid using the inherently mass and linear-correlation preserving CSLAM al-
232 gorithm. Note that in CAM-SE-CSLAM the dry mass internally predicted by CSLAM, $\Delta p^{(cslam)}$,
233 is, by design, equal to $\Delta p^{(gll)}$ integrated over the CSLAM/physics grid control volume (Lauritzen
234 et al. 2017). Since the tracer grid and physics grids are co-located and $\Delta p^{(pg)} = \Delta p^{(cslam)}$ then the
235 mass conservation, correlation preservation, consistency and shape-preservation constraints are
236 inherently fulfilled.

237 *b. Mapping tendencies from physics grid (pg) to dynamics grid (GLL)*

238 The physics tendencies are computed on the finite-volume physics grid and are denoted
239 $f_T^{(pg)}, f_u^{(pg)}, f_v^{(pg)}$, and $f_m^{(pg)}$. Note that dry air mass is not modified by physics and hence there
240 is no tendency for dry mass, $f_{\Delta p} \equiv 0$. Also, it is important to map tendencies and not state from
241 the physics grid to GLL grid otherwise one will get spurious tendencies from mapping errors when
242 the actual physics tendency is zero (unless a reversible map is used).

243 It is important that this process:

- 244 1. for tracers; mass tendency is conserved,

- 245 2. for tracers; in each tracer grid cell the mass tendency from physics must not exceed tracer
246 mass available in tracer grid cell (it is assumed that the physics tendency will not drive tracer
247 mixing ratio negative on the physics grid),

248 3. linear correlation preservation,

249 4. consistency, i.e., the mapping preserves a constant tendency.

250 Other properties that may be important, but not pursued here, includes total energy conservation
251 (incl. components of total energy) and axial angular momentum conservation. Scalar variables
252 are mapped from the physics grid to GLL grid using a tensor-product Lagrange interpolation in
253 two dimensions (i.e., we assume that the pressure variations in the vertical are small). The local
254 coordinates on a cubed-sphere are discontinuous at the element edges so the interpolation requires
255 special attention at the cube corners and edges. The details are provided in the Appendix. Lagrange
256 interpolation preserves a constant (including zero) and linear correlations. Tracer and physics grids
257 are co-located so tracer mass, tracer shape, and tracer correlations are trivially preserved on the
258 tracer grid; and the inconsistency in point 2 above will not appear.

259 Mapping from pg to GLL grids while conserving mass was found to be difficult without ex-
260 cessive grid imprinting at element edges. Mass-conservation (using conventional finite-volume
261 methods) requires a control volume to be defined around the GLL points (see Figure 4 in this
262 paper or Figure 8b in Ullrich et al. 2016). These volumes are artificial and not consistent with
263 the SE method. Integrating the CSLAM reconstruction of water tracers of such artificial control
264 volumes led to GLL node grid imprinting in the mapping and will not preserve a constant mixing
265 ratio since the mapping of $\Delta p^{(pg)}$ to GLL will not yield the GLL node value for dry pressure-level
266 thickness (i.e., the maps are not reversible). A reversible map requires that the number of degrees
267 of freedom on the source mesh ($pg3$ has 9 degrees of freedom) equal the number of degrees of

268 freedom on the target mesh ($np4$ grid has 16 degrees of freedom). This condition is violated by
269 construction for individual elements.

270 It was also found important to use an interpolator that is smooth across element boundaries.

271 Using an algorithm that only uses information from an element or control volumes will (at best)
272 be C^0 at the element boundaries and therefore lead to boundary node grid imprinting. A stencil that
273 extends beyond one element is therefore necessary. After much experimentation, the best results
274 in terms of grid-imprinting were obtained with tensor-cubic interpolation (see the Appendix for
275 details) and by using the CAM-SE-CSLAM configuration (which requires the same boundary
276 exchange/communication as used in CSLAM).

277 *c. Time splitting and physics-dynamics coupling*

278 The physics and dynamics are integrated in time using a sequential-update approach (e.g.,
279 Williamson 2002). The dynamical core is sub-cycled over the (usually) longer physics time-step,
280 Δt_{phys} , e.g., the vertical remapping time-step Δt_{remap} is cycled $nsplit$ times, totaling to Δt_{phys} . In
281 CAM-SE, a fraction of the physics forcing, e.g., $f_q \times \Delta t_{remap}$ is applied at the beginning of each
282 $nsplit$ vertical remap subcycles, such that the full forcing ($f_q \times \Delta t_{phys}$) is realized over the course
283 of a physics time-step. This approach of dribbling the tendencies over sub-intervals has the ad-
284 vantage of reducing gravity wave noise (Thatcher and Jablonowski 2016), but may disrupt tracer
285 mass conservation (Zhang et al. 2017). In CAM-SE-CSLAM, all but the tracer mass quantities are
286 dribbled, with tracer mass receiving the full physics update, e.g., $f_q \times \Delta t_{phys}$, applied only at the
287 beginning of the first remap sub-cycle, and thereby conserving tracer mass. This is the $ftype = 2$
288 configuration described in detail in Section 3.6.3 in Lauritzen et al. (2018).

289 In the SE integration of the equations of motion on the GLL grid the water species are
290 needed in the computation of the pressure gradient force and generalized expressions for heat

capacity at constant pressure c_p , etc. Hence the mixing ratios for water vapor and dynamically/thermodynamically active condensates (e.g., cloud liquid and cloud ice) are needed on the GLL grid. We have chosen to advect the water species on the GLL grid using the SE method as well as on the physics grid using CSLAM. Every time physics updates the water species on the CSLAM grid, a forcing term (equal to the difference between updated CSLAM water variables and the SE values) is applied to the GLL water variables using dribbling so that the CSLAM solution and SE solution for water species are tightly coupled.

4. Results

A hierarchy of idealized model configurations are presented in order to elucidate the differences between CAM-SE and CAM-SE-CSLAM (available from the CESM2.1 release; <https://doi.org/10.5065/D67H1H0V>). Here, the configurations are presented in order of increasing complexity, each with a pair of approximately 1° simulations, pertaining to the *ne30np4* (CAM-SE) and *ne30pg3* (CAM-SE-CSLAM) grids, and a $\Delta t_{phys} = 1800$ s.

a. Moist Baroclinic Wave

The moist baroclinic wave test case was developed as part of the ‘CESM Simple Models’ project (Polvani et al. 2017), and included in the release of CESM2. It is effectively the dry test-case of Ullrich et al. (2014), but initialized with moisture and coupled to the Kessler moist physics routine (Kessler 1969). For more details on this test case (which was part of the 2016 Dynamical Core Model Intercomparison Project, Ullrich et al. 2017), see Section 4.1 in Lauritzen et al. (2018). A measure of the uncertainty in the reference solution, the L_2 difference norm between two high-resolution solutions using different dynamical cores, was also presented in Lauritzen et al. (2018)

312 and provided again here in Figure 6. The L_2 norm between CAM-SE and CAM-SE-CSLAM lies
313 below the uncertainty of the reference solution, indicating their differences are insignificant.

314 The flow field of the baroclinic wave test is used to drive the terminator “toy”-chemistry test of
315 Lauritzen et al. (2015b, 2017). The terminator test is used to assess linear-correlation preservation
316 using two reactive species advected across the terminator line. The model is initialized with species
317 for which their weighted sum, Cl_y , is a constant (constant surface pressure and constant mixing
318 ratio; $Cl_y = Cl + 2Cl_2 = 4 \times 10^{-6} \text{ kg/kg}$), such that if tracer correlations are preserved, then the
319 column-integrated weighted sum of the species should not vary in time. Figure 7 provides a
320 snapshot of the vertically integrated weighted sum of species at day 15. In CAM-SE, the tracer
321 correlations are not preserved at day 15 and the field is populated by overshoots and undershoots.
322 In contrast, by day 15, CAM-SE-CSLAM still conserves tracer correlations to within machine
323 precision, consistent with the previous results of this test-case initialized with a dry baroclinic
324 wave (Lauritzen et al. 2017).

325 b. *Aqua-planets*

326 Two year long aqua-planet simulations are performed using CAM-SE and CAM-SE-CSLAM,
327 using the CAM4 physics package (Neale et al. 2010), as discussed in Section 2. Away from the
328 grid-scale, the mean states in the two models are very similar. Figure 8 shows the zonal-mean cli-
329 matological precipitation rates in CAM-SE and CAM-SE-CSLAM. Considering how sensitive this
330 aqua-planet configuration is to design choices in CAM-SE (Lauritzen et al. 2018), it is somewhat
331 unexpected that the zonal means look so similar to one another.

332 A plot similar to Figure 3a is constructed for the CAM-SE-CSLAM simulation, a probability
333 density distribution of upward ω conditionally sampled based on location within the element. Like
334 Figure 3a, Figure 3b divides up the control volumes by corner, edge and interior cells. Through the

335 use of the quasi-equal area physics grid, the dynamical core state appears more or less independent
336 of location within the element, a marked improvement over CAM-SE. Since the state is approxi-
337 mately independent of in-element location, it follows that the physics forcing, which is evaluated
338 from the dynamical core state, may be expected to also show an improvement in grid-imprinting.

339 The low-level, mean and variance of the temperature tendencies from the physics, on the GLL
340 grid, $f_T^{(gll)}$, in the two simulations are shown in Figure 9. The mean states in the two models
341 resemble one another, consistent with the zonal mean precipitation rates (Figure 8). The mean
342 physics tendencies contains modest grid imprinting in CAM-SE (barely visible near the storm-
343 track regions), while in the variance field, grid imprinting is both ubiquitous and unmistakable.
344 The variance is larger on boundary nodes, manifesting as a ‘stitching’ pattern resembling the
345 cube-sphere grid. In CAM-SE-CSLAM, the grid imprinting is all but eliminated based on the
346 mean and variance of the physics tendencies (Figure 9), consistent with our expectation.

347 The global mean and variance of the low-level physics tendencies are marginally lower in CAM-
348 SE-CSLAM compared with CAM-SE on the GLL grid (by about 1% and 6% for the mean and
349 variance, respectively; Figure 9). While these differences may be small, and potentially insignifi-
350 cant, they are consistent with the state on the GLL grid in the two simulations. Through re-creating
351 Figure 3a, but using the ω field on the GLL grid in the CAM-SE-CSLAM run, the frequency of
352 large magnitude ω values (less than -1.0 Pa/s) associated with interior, corner and edge nodes is
353 slightly lower (not shown). This suggests that the lower magnitude physics forcing in CAM-SE-
354 CSLAM impacts the state on the GLL grid, albeit modestly. Therefore the lower frequency of
355 large magnitude ω in CAM-SE-CSLAM (Figure 3) may not be solely due to the smoothing ef-
356 fect of integrating the basis functions over control volumes, but also the lower magnitude physics
357 tendencies feeding back onto the dynamical state.

358 As stated in Section 3, the mapping of the state to the physics grid and the reverse interpolation
359 of physics tendencies to the GLL grid is not total energy conserving. CAM has a global energy
360 fixer (Williamson et al. 2015) which can be used to estimate the errors associated with the mapping
361 algorithms. To do so, it is presumed that there are no compensating mapping errors in going to
362 and from the physics and dynamics grids, and that CAM-SE-CSLAM and CAM-SE have the same
363 energy dissipation rates. Under these assumptions the spurious globally integrated total energy
364 errors due to the mapping algorithm is estimated to be approximately 0.0025 W/m^2 in the aqua-
365 planet simulations. In comparison, the dynamical core total energy dissipation is on the order of
366 0.1 W/m^2 (Lauritzen et al. 2018).

367 *c. Held-Suarez with Topography*

368 Grid imprinting associated with the flow around obstacles is more problematic than that en-
369 countered on the aqua-planets. In order to diagnose grid imprinting due to topographic flow, an
370 idealized Held-Suarez configuration (Held and Suarez 1994) is outfitted with real world topogra-
371 phy after Fox-Rabinovitz et al. (2000); Baer et al. (2006), and run for two years. Figure 10 shows
372 the mean ω at two different vertical levels in the middle troposphere. The data are presented as a
373 raster plot on their respective unstructured grids, in order to delineate whether a particular value is
374 associated with an interior, edge or element boundary node.

375 At higher latitudes (e.g., the southern Andes), the flow is smooth, conforming reasonably to
376 the underlying topography. At lower latitudes, over the Andes (between the equator and 20°S)
377 or the Himalayas (from 20°N to 30°N), there is a clear preference for extrema to occur at the
378 element boundaries (Figure 10). The vertical structure of ω in regions of strong grid-imprinting
379 indicates full-troposphere upward/downward motion (not shown). Grid imprinting is therefore
380 more common in regions of weak stratification, such as occurs in the deep tropics, with forced up-

381 slope flow facilitating the release of gravitational instability. Resolved updrafts/downdrafts often
382 align with the element boundaries due to its systematically tighter pressure gradients.

383 Through the use of the quasi-equal area physics grid, grid imprinting due to topographic flow
384 is reduced (Figures 10). The native topography lives on the physics grid, and the topography is
385 mapped to the nodal points at run-time in CAM-SE-CSLAM. Mapping topography to the quadra-
386 ture nodes ensures that no new extrema will be introduced to the boundary nodes, where the
387 solution is least smooth. This effect can not be very large, since grid noise over topography is
388 similar in CAM-SE and CAM-SE-CSLAM on the GLL grid (not shown). From the perspective
389 of the physics grid, CAM-SE-CSLAM clearly mitigates the influence of grid-induced extrema on
390 the state. This can be seen by comparing Figures 10a and 10b, and their differences (Figure 10c),
391 which shows that the largest differences coincide with the element boundaries. The reduction in
392 grid imprinting in this modified Held-Suarez configuration appears to be almost entirely a result
393 of the smoothing effect of integrating the basis functions over the control volumes of the physics
394 grid.

395 *d. AMIP type simulations*

396 A pair of 20 year-long AMIP type simulations are performed, using CAM, version 6 physics
397 package (CAM6) and using perpetual year 2000 SST boundary conditions (*F2000climo* compset
398 in CESM2.0; <https://doi.org/10.5065/D67H1H0V>). Figure 11 shows the climatological pre-
399 cipitation fields in CAM-SE (left) and CAM-SE-CSLAM (middle), and over the same mountain-
400 ous regions as in Figure 10. The plots have some similar features to the ω field in the Held-Suarez
401 runs; the greater variance at lower latitudes, and on the windward side of the mountains are broadly
402 similar. CAM-SE-CSLAM has a lower spatial variance, e.g., the lack of extrema over the Andes
403 at about 15° S compared to CAM-SE, and the grid-scale precipitation peak over the Himalayas

404 at about 30° N. The difference plot (Figure 11; right panel) is more broadly populated by blue,
405 purple and white contours, indicating that CAM-SE has, in general, larger magnitude precipitation
406 rates over high topography. The difference plots also highlight a couple of zonally aligned strips
407 of anomalous precipitation, in particular, near the foot of the Himalayas in CAM-SE. These bands
408 are in the same location as the bands of precipitation identified in CAM-SE in Lauritzen et al.
409 (2015a) (their Figure 7), but using CAM, version 5 physics, of which they argue are spurious in
410 nature.

411 To assist in identifying whether a particular precipitation pattern is spurious, an *F2000climo*
412 simulation is carried out using the finite-volume dynamical core that uses a regular latitude-
413 longitude $0.9^{\circ} \times 1.25^{\circ}$ grid (CAM-FV; *f09* grid; Neale et al. 2012). CAM-FV is the default
414 low resolution model in CESM2.0, and with its smoothly varying grid, does not suffer from the
415 Quadrature Node Problem (Section 2). Figure 12 shows the global precipitation fields in CAM-SE,
416 CAM-SE-CSLAM and CAM-FV, compared to an observational dataset, the Global Precipitation
417 Climatology Project (GPCP; 1979-2003) gridded dataset (Huffman et al. 2001). The magnitude
418 of the precipitation rates in all three models are higher than the GPCP dataset, primarily over land
419 in the Tropics (note the lack of red contours in the GPCP dataset), which should be interpreted
420 cautiously due to widely-accepted issues in constructing a reliable, gridded, global precipitation
421 dataset. At lower latitudes, CAM-FV has lower spatial variance, and overall lower magnitudes,
422 compared with CAM-SE. The GPCP dataset indicates that perhaps the precipitation rates in low-
423 latitude mountainous regions in CAM-FV and CAM-SE are larger than in reality. Following suit,
424 the reduction in magnitude and spatial variance in precipitation in these regions in CAM-SE-
425 CSLAM may be interpreted as an improvement over CAM-SE.

426 **5. Conclusions**

427 Element-based high-order Galerkin Methods possess many of the attractive qualities recom-
428 mended for next generation global atmospheric models. Among these, high-order accuracy is
429 achieved with minimal communication between elements, allowing for near perfect scaling on
430 massively parallel systems. Element communication amounts to a numerical flux applied to the
431 element boundaries, reconciling overlapping solutions of adjacent elements but degrading the
432 smoothness of the boundary nodes in the process (to C^0). For non-smooth problems, gradients are
433 systematically tighter at the element boundaries, and local extrema often characterize the boundary
434 nodes. This behavior is illustrated using NCAR’s Community Atmosphere Model with Spectral
435 Elements dynamics (CAM-SE) in an aqua-planet configuration, in a Held-Suarez configuration
436 with real-world topography and in an AMIP type configuration.

437 The authors argue that the conventional physics-dynamics coupling paradigm, in which the
438 physical parameterizations are evaluated on the dynamical core grid, exacerbates grid imprinting.
439 A separate physics grid is proposed and implemented in CAM-SE, and referred to as CAM-SE-
440 CSLAM, through dividing the elements into quasi-equal areas with equivalent degrees of freedom.
441 The state is mapped to the physics grid with high-order accuracy through integrating CAM-SE’s
442 Lagrange basis functions over the control volumes. Control volumes near element boundaries now
443 represent a state in the vicinity of the extrema produced through the boundary exchange, as op-
444 posed to the the nodal value itself. These control volumes are also compatible with a ‘large-scale
445 state’ as required by the physical parameterizations. The physical parameterizations are evalu-
446 ated on the finite volume grid, and the forcing terms are mapped back to the dynamical core grid
447 using a cubic tensor-product Lagrange interpolation. In aqua-planet simulations, evaluating the
448 parameterizations on the physics grid removes any obvious dependence of proximity to the ele-

449 ment boundary, resulting in a more realistic state with negligible grid imprinting. The mapping
450 algorithm does not conserve total energy, but it is estimated that these errors are one to two orders
451 of magnitude less than the total energy dissipation from the dynamical core.

452 In CAM-SE-CSLAM, the physics grid replaces the default CAM-SE quadrature point-based
453 coupler grid (Figure 4) to compute fluxes between model components in the Community Earth
454 System Model (CESM). The appeal here is two-fold. Through integrating the Lagrange basis
455 functions over control volumes, one can be certain that the fluxes computed from this grid are a
456 volume averaged flux. The same can not be said for CAM-SE, where artificial control volumes
457 (with sizes proportional quadrature weights) are constructed around nodal values and assumed to
458 represent the volume averaged state. The second advantage of the new coupler grid is that extrema
459 occurring on boundary nodes may no longer influence other model components in simulations
460 without rough topography. While grid imprinting is effectively eliminated in the aqua-planets,
461 experiments with real-world topography (Held-Suarez and AMIP type configurations) reduces,
462 but does not entirely eliminate, imprinting from the mean state. The quasi-equal area physics grid
463 is nonetheless effective at mitigating numerical nuances associated with high-order element-based
464 Galerkin methods, for non-smooth problems.

465 Future work will focus on the impact of using a coarser, $pg \times pg = 2 \times 2$ physics grid configu-
466 ration. The coarser physics grid may be more effective at reducing spurious noise over regions of
467 rough topography, while potentially reducing the computational overhead. Any advantages of us-
468 ing a coarser resolution physics grid will be weighed against any potential reduction in a model's
469 effective resolution.

470 *Acknowledgments.* NCAR is sponsored by the National Science Foundation (NSF). We thank
471 three anonymous reviewers for their helpful comments that significantly improved the clarity of

472 the manuscript. Herrington thanks NCAR’s Computational and Information Systems Laboratory
 473 (CISL) and NCAR’s Climate and Global Dynamics division (CGD) for computational resources
 474 and technical support. Herrington, Reed, and Lauritzen are grateful to the NCAR Advanced Study
 475 Program graduate visitor program for funding Herrington’s 12-month visit. Goldhaber was par-
 476 tially supported by the Accelerated Climate Modeling for Energy (ACME) project, and work pack-
 477 age 12 – 015334 “Multiscale Methods for Accurate, Efficient, and the Accelerated Scale-Aware
 478 Models, both funded through the U.S. Department of Energy Office of Biological and Environ-
 479 mental Research. Goldhaber is also partially supported through NSF award AGS-1500187 “De-
 480 velopment and Testing of a Global Quasi 3-D multi Modeling Framework.” Model source code is
 481 officially released with CESM2.1 (<https://doi.org/10.5065/D67H1H0V>).

APPENDIX

482 The mapping of the physics tendencies from the physics grid to the GLL grid is done with
 483 tensor-cubic Lagrange interpolation. The elements of the cubed-sphere in SE are created
 484 from an equi-angular gnomonic projection. Consider one element $(\alpha, \beta) \in [\alpha_1^{(elem)}, \alpha_2^{(elem)}] \times$
 485 $[\beta_1^{(elem)}, \beta_2^{(elem)}]$, where (α, β) are central angle coordinates and $\alpha_1^{(elem)}$ and $\alpha_2^{(elem)}$ are the min-
 486 imum and maximum central angles in the α -coordinate direction, respectively, and similarly for
 487 β . Let $\Delta\alpha^{(elem)} = \alpha_2^{(elem)} - \alpha_1^{(elem)}$ and $\Delta\beta^{(elem)} = \beta_2^{(elem)} - \beta_1^{(elem)}$. The physics grid cell central
 488 angle centers are located at
 489

$$(\alpha_i^{(pg)}, \beta_j^{(pg)}) = \left[\alpha_1^{(elem)} + (i - \frac{1}{2}) \Delta\alpha^{(pg)}, \beta_1^{(elem)} + (j - \frac{1}{2}) \Delta\beta^{(pg)} \right], \quad (\text{A1})$$

490 where $\Delta\alpha^{(pg)} = \Delta\beta^{(pg)} = \frac{\Delta\alpha^{(elem)}}{pg} = \frac{\Delta\beta^{(elem)}}{pg}$. The interpolation is performed in central-angle co-
 491 ordinates using tensor product cubic interpolation. For elements located on a cubed-sphere edge

or corner the coordinate system for neighboring elements may be on a different panel. To take into account this coordinate change the central angle locations of physics grid cell centers located on other panels are transformed to the coordinate system of the panel the element in question is located on (the transformations are given in, e.g., Nair et al. 2005). An illustration is given in Figure 13 for an element located in the lower left corner of a panel. The element in question is $(\xi, \chi) \in (-1, 1)^2$ where, for simplicity, we have transformed the element coordinates into normalized coordinates $(\xi, \chi) = \left(\frac{2(\alpha^{(pg)} - \alpha_1^{(elem)})}{\Delta\alpha^{(elem)}} - 1, \frac{2(\beta^{(pg)} - \beta_1^{(elem)})}{\Delta\beta^{(elem)}} - 1 \right)$; also used internally in the SE dynamical core (see, e.g., section 3.3 in Lauritzen et al. 2018). The GLL points are located at $-1, -1/\sqrt{1}, 1/\sqrt{5}$, and 1 in each coordinate direction. Near the edges/corners of an element cubic extrapolation is used if the centered stencil expands beyond the panel.

References

- Arakawa, A., and W. H. Schubert, 1974: Interaction of a cumulus cloud ensemble with the large-scale environment, Part I. *J. Atmos. Sci.*, **31**, 674–701.
- Bacmeister, J. T., K. A. Reed, C. Hannay, P. Lawrence, S. Bates, J. E. Truesdale, N. Rosenbloom, and M. Levy, 2018: Projected changes in tropical cyclone activity under future warming scenarios using a high-resolution climate model. *Climatic Change*, **146**, 547–560, doi: 10.1007/s10584-016-1750-x, URL <http://dx.doi.org/10.1007/s10584-016-1750-x>.
- Baer, F., H. Wang, J. J. Tribbia, and A. Fournier, 2006: Climate modeling with spectral elements. *Mon. Wea. Rev.*, **134**, 3610–3624, doi:10.1175/MWR3360.1, URL <http://dx.doi.org/10.1175/MWR3360.1>.
- Brdar, S., M. Baldauf, A. Dedner, and R. Klöfkorn, 2013: Comparison of dynamical cores for nwp models: comparison of cosmo and dune. *Theoretical and Computational Fluid Dynamics*,

- 514 **27 (3-4)**, 453–472, doi:10.1007/s00162-012-0264-z.
- 515 Canuto, C., M. Y. Hussaini, A. Quarteroni, and T. Zang, 2007: *Spectral Methods: Evolution to*
516 *Complex Geometries and Applications to Fluid Dynamics*. 1st ed., Springer.
- 517 Dennis, J. M., and Coauthors, 2012: CAM-SE: A scalable spectral element dynamical core for
518 the Community Atmosphere Model. *Int. J. High. Perform. C.*, **26 (1)**, 74–89, doi:10.1177/
519 1094342011428142, URL <http://hpc.sagepub.com/content/26/1/74.abstract>, <http://hpc.sagepub.com/content/26/1/74.full.pdf+html>.
- 520
- 521 Durran, D., 2010: *Numerical Methods for Fluid Dynamics: With Applications to Geophysics*,
522 Texts in Applied Mathematics, Vol. 32. 2nd ed., Springer, 516 p.
- 523 Fournier, A., M. A. Taylor, and J. J. Tribbia, 2004: The spectral element atmosphere model
524 (SEAM): High-resolution parallel computation and localized resolution of regional dynamics.
525 *Mon. Wea. Rev.*, **132 (3)**, 726–748.
- 526 Fox-Rabinovitz, M. S., G. L. Stenchikov, M. J. Suarez, L. L. Takacs, and R. C. Govindaraju, 2000:
527 A uniform- and variable-resolution stretched-grid gcm dynamical core with realistic orography.
528 *Mon. Wea. Rev.*, **128**, 1883–1898.
- 529 Giraldo, F., and M. Restelli, 2008: A study of spectral element and discontinuous galerkin methods
530 for the Navier-Stokes equations in nonhydrostatic mesoscale atmospheric modeling: Equation
531 sets and test cases. *J. Comput. Phys.*, **227 (8)**, 3849 – 3877, doi:<http://dx.doi.org/10.1016/j.jcp.2007.12.009>.
- 532
- 533 Guba, O., M. Taylor, and A. St-Cyr, 2014a: Optimization-based limiters for the spectral element
534 method. *J. Comput. Phys.*, **267 (0)**, 176 – 195, doi:<http://dx.doi.org/10.1016/j.jcp.2014.02.029>.

- 535 Guba, O., M. A. Taylor, P. A. Ullrich, J. R. Overfelt, and M. N. Levy, 2014b: The spectral element
536 method (sem) on variable-resolution grids: evaluating grid sensitivity and resolution-aware nu-
537 matical viscosity. *Geosci. Model Dev.*, **7** (6), 2803–2816, doi:10.5194/gmd-7-2803-2014.
- 538 Held, I. M., and M. J. Suarez, 1994: A proposal for the intercomparison of the dynamical cores of
539 atmospheric general circulation models. *Bull. Am. Meteorol. Soc.*, **73**, 1825–1830.
- 540 Huffman, G. J., R. F. Adler, M. M. Morrissey, D. T. Bolvin, S. Curtis, R. Joyce, B. McGavock,
541 and J. Susskind, 2001: Global precipitation at one-degree daily resolution from multisatellite
542 observations. *J. Hydrometeorology*, **2** (1), 36–50.
- 543 Kessler, E., 1969: On the distribution and continuity of water substance in atmospheric circula-
544 tions. *Meteorol. Monogr.*, **10** (32), 88.
- 545 Kim, Y.-J., F. X. Giraldo, M. Flatau, C.-S. Liou, and M. S. Peng, 2008: A sensitivity study of the
546 kelvin wave and the Madden-Julian oscillation in aquaplanet simulations by the Naval Research
547 Laboratory Spectral Element Atmospheric Model. *J. Geo. Res.: Atmospheres*, **113** (D20), doi:
548 10.1029/2008JD009887, d20102.
- 549 Lauritzen, P., and J. Thuburn, 2012: Evaluating advection/transport schemes using interrelated
550 tracers, scatter plots and numerical mixing diagnostics. *Quart. J. Roy. Met. Soc.*, **138** (665),
551 906–918, doi:10.1002/qj.986.
- 552 Lauritzen, P. H., J. T. Bacmeister, P. F. Callaghan, and M. A. Taylor, 2015a: Ncar global model
553 topography generation software for unstructured grids. *Geoscientific Model Development Dis-
554 cussions*, **8** (6), 4623–4651, doi:10.5194/gmdd-8-4623-2015.

- 555 Lauritzen, P. H., A. J. Conley, J.-F. Lamarque, F. Vitt, and M. A. Taylor, 2015b: The terminator
556 "toy" chemistry test: a simple tool to assess errors in transport schemes. *Geoscientific Model*
557 *Development*, **8** (5), 1299–1313, doi:10.5194/gmd-8-1299-2015.
- 558 Lauritzen, P. H., M. A. Taylor, J. Overfelt, P. A. Ullrich, R. D. Nair, S. Goldhaber, and
559 R. Kelly, 2017: CAM-SE-CSLAM: Consistent coupling of a conservative semi-lagrangian
560 finite-volume method with spectral element dynamics. *Mon. Wea. Rev.*, **145** (3), 833–855, doi:
561 10.1175/MWR-D-16-0258.1.
- 562 Lauritzen, P. H., and Coauthors, 2018: NCAR CESM2.0 release of CAM-SE: A reformulation
563 of the spectral-element dynamical core in dry-mass vertical coordinates with comprehensive
564 treatment of condensates and energy. *J. Adv. Model. Earth Syst.*, doi:10.1029/2017MS001257.
- 565 Lin, S.-J., 2004: A 'vertically Lagrangian' finite-volume dynamical core for global models. *Mon.*
566 *Wea. Rev.*, **132**, 2293–2307.
- 567 Maday, Y., and A. T. Patera, 1987: Spectral element methods for the incompressible Navier Stokes
568 equations. *State of the Art Surveys on Computational Mechanics*, A. K. Noor, and J. T. Oden,
569 Eds., ASME, New York, 71–143.
- 570 Medeiros, B., D. L. Williamson, and J. G. Olson, 2016: Reference aquaplanet climate in the
571 community atmosphere model, version 5. *J. Adv. Model. Earth Syst.*, **8** (1), 406–424, doi:10.
572 1002/2015MS000593.
- 573 Nair, R., H.-W. Choi, and H. Tufo, 2009: Computational aspects of a scalable high-order dis-
574 continuous galerkin atmospheric dynamical core. *Computers & Fluids*, **38** (2), 309 – 319, doi:
575 <http://dx.doi.org/10.1016/j.compfluid.2008.04.006>.

- 576 Nair, R. D., M. N. Levy, and P. H. Lauritzen, 2011: Emerging numerical methods for atmo-
577 spheric modeling, in: P.H. Lauritzen, R.D. Nair, C. Jablonowski, M. Taylor (Eds.), Numerical
578 techniques for global atmospheric models. *Lecture Notes in Computational Science and Engi-*
579 *neering, Springer*, **80**.
- 580 Nair, R. D., S. J. Thomas, and R. D. Loft, 2005: A discontinuous galerkin transport scheme on the
581 cubed sphere. *Mon. Wea. Rev.*, **133** (4), 814–828, doi:10.1175/MWR2890.1.
- 582 Neale, R. B., and B. J. Hoskins, 2000: A standard test for agcms including their physical
583 parametrizations: I: the proposal. *Atmos. Sci. Lett.*, **1** (2), 101–107, doi:10.1006/asle.2000.0022.
- 584 Neale, R. B., and Coauthors, 2010: Description of the NCAR Community Atmosphere Model
585 (CAM 4.0). NCAR Technical Note, National Center of Atmospheric Research.
- 586 Neale, R. B., and Coauthors, 2012: Description of the NCAR Community Atmosphere Model
587 (CAM 5.0). NCAR Technical Note NCAR/TN-486+STR, National Center of Atmospheric Re-
588 search.
- 589 Plant, R. S., and G. C. Craig, 2008: A stochastic parameterization for deep convection based
590 on equilibrium statistics. *J. Atmos. Sci.*, **65**, 87–105, doi:10.1175/2007JAS2263.1, URL <http://dx.doi.org/10.1175/2007JAS2263.1>.
- 592 Polvani, L., A. Clement, B. Medeiros, J. Benedict, and I. Simpson, 2017: Opening the door to
593 simpler climate models in the community earth system model project. *EOS*, submitted.
- 594 Putman, W. M., and S.-J. Lin, 2007: Finite-volume transport on various cubed-sphere grids. *J.*
595 *Comput. Phys.*, **227** (1), 55–78.
- 596 Reed, K. A., J. T. Bacmeister, N. A. Rosenbloom, M. F. Wehner, S. C. Bates, P. H. Lauritzen,
597 J. E. Truesdale, and C. Hannay, 2015: Impact of the dynamical core on the direct simulation

- 598 of tropical cyclones in a high-resolution global model. *Geophys. Res. Lett.*, **42** (9), 3603–3608,
599 doi:10.1002/2015GL063974.
- 600 Rhoades, A. M., X. Huang, P. A. Ullrich, and C. M. Zarzycki, 2016: Characterizing sierra
601 nevada snowpack using variable-resolution cesm. *Journal of Applied Meteorology and Cli-*
602 *matology*, **55** (1), 173–196, doi:10.1175/JAMC-D-15-0156.1, URL <https://doi.org/10.1175/JAMC-D-15-0156.1>.
- 603 Simmons, A. J., and D. M. Burridge, 1981: An energy and angular-momentum conserving vertical
604 finite-difference scheme and hybrid vertical coordinates. *Mon. Wea. Rev.*, **109** (4), 758–766.
- 605 Small, R. J., and Coauthors, 2014: A new synoptic scale resolving global climate simulation
606 using the community earth system model. *J. Adv. Model. Earth Syst.*, **6** (4), 1065–1094, doi:
607 10.1002/2014MS000363.
- 608 Suarez, M. J., A. Arakawa, and D. A. Randall, 1983: The parameterization of the planetary
609 boundary layer in the ucla general circulation model: Formulation and results. *Mon. Wea. Rev.*,
610 **111** (11), 2224–2243.
- 611 Taylor, M., J. Edwards, and A. St-Cyr, 2008: Petascale atmospheric models for the community
612 climate system model: new developments and evaluation of scalable dynamical cores. *J. Phys.:
613 Conf. Ser.*, **125**, doi:10.1088/1742-6596/125/1/012023.
- 614 Taylor, M. A., and A. Fournier, 2010: A compatible and conservative spectral element method on
615 unstructured grids. *J. Comput. Phys.*, **229** (17), 5879 – 5895, doi:10.1016/j.jcp.2010.04.008.
- 616 Thatcher, D. R., and C. Jablonowski, 2016: A moist aquaplanet variant of the Held–Suarez test
617 for atmospheric model dynamical cores. *Geoscientific Model Development*, **9** (4), 1263–1292,
618 doi:10.5194/gmd-9-1263-2016, URL <https://www.geosci-model-dev.net/9/1263/2016/>.

- 620 Ullrich, P. A., 2014: A global finite-element shallow-water model supporting continuous and dis-
621 continuous elements. *Geosci. Model Dev.*, **7** (6), 3017–3035, doi:10.5194/gmd-7-3017-2014.
- 622 Ullrich, P. A., D. Devendran, and H. Johansen, 2016: Arbitrary-order conservative and consistent
623 remapping and a theory of linear maps: Part ii. *Mon. Wea. Rev.*, **144** (4), 1529–1549, doi:
624 10.1175/MWR-D-15-0301.1.
- 625 Ullrich, P. A., T. Melvin, C. Jablonowski, and A. Staniforth, 2014: A proposed baroclinic wave test
626 case for deep and shallow-atmosphere dynamical cores. *Quart. J. Royal Meteor. Soc.*, **140** (682),
627 1590–1602.
- 628 Ullrich, P. A., and M. A. Taylor, 2015: Arbitrary-order conservative and consistent remap-
629 ping and a theory of linear maps: Part I. *Mon. Wea. Rev.*, **143**, 2419–2440, doi:10.1175/
630 MWR-D-14-00343.1.
- 631 Ullrich, P. A., and Coauthors, 2017: "dcmip2016: A review of non-hydrostatic dynamical core
632 design and intercomparison of participating models". *Geosci. Model Dev.*, **10**, 4477–4509, doi:
633 10.5194/gmd-10-4477-2017.
- 634 Wan, H., and Coauthors, 2013: "the icon-1.2 hydrostatic atmospheric dynamical core on triangular
635 grids, part i: formulation and performance of the baseline version". *Geosci. Model Dev.*, **6**, 735–
636 763.
- 637 Wedi, N. P., 2014: Increasing horizontal resolution in numerical weather prediction and climate
638 simulations: illusion or panacea? *Philosophical Transactions of the Royal Society of London A:*
639 *Mathematical, Physical and Engineering Sciences*, **372** (2018), doi:10.1098/rsta.2013.0289.
- 640 Williamson, D. L., 1999: Convergence of atmospheric simulations with increasing horizontal res-
641 olution and fixed forcing scales. *Tellus A*, **51**, 663–673, doi:10.1034/j.1600-0870.1999.00009.x.

- 642 Williamson, D. L., 2002: Time-split versus process-split coupling of parameterizations and dy-
643 namical core. *Mon. Wea. Rev.*, **130**, 2024–2041.
- 644 Williamson, D. L., J. G. Olson, C. Hannay, T. Toniazzo, M. Taylor, and V. Yudin, 2015: Energy
645 considerations in the community atmosphere model (cam). *J. Adv. Model. Earth Syst.*, **7** (3),
646 1178–1188, doi:10.1002/2015MS000448, URL <http://dx.doi.org/10.1002/2015MS000448>.
- 647 Zarzycki, C. M., C. Jablonowski, and M. A. Taylor, 2014a: Using variable-resolution meshes to
648 model tropical cyclones in the community atmosphere model. *Mon. Wea. Rev.*, **142** (3), 1221–
649 1239, doi:10.1175/MWR-D-13-00179.1.
- 650 Zarzycki, C. M., M. N. Levy, C. Jablonowski, J. R. Overfelt, M. A. Taylor, and P. A. Ullrich,
651 2014b: Aquaplanet experiments using cam’s variable-resolution dynamical core. *J. Climate*,
652 **27** (14), 5481–5503, doi:10.1175/JCLI-D-14-00004.1.
- 653 Zhang, K., and Coauthors, 2017: Impact of numerical choices on water conservation in the e3sm
654 atmosphere model version 1 (eam v1). *Geoscientific Model Development Discussions*, **2017**,
655 1–26, doi:10.5194/gmd-2017-293.

656 LIST OF FIGURES

657	Fig. 1.	Example of CAM-SE GLL quadrature grids, marked with red filled circles, (a & c) on the cubed-sphere and (b & d) in an element. (a)-(b) and (c)-(d) use 4×4 ($np = 4$) and 8×8 ($np = 8$) GLL quadrature points in each element, respectively. (a) and (c) have the same average grid-spacing at the Equator (7.5°) which is obtained by using (a) 4×4 ($ne = 4$) and (b) 2×2 ($ne = 2$) elements on each cubed-sphere face/panel, respectively. The element boundaries are marked with thick light blue lines. The grid configurations shown on (a) and (c) are referred to as $ne4np4$ and $ne2np8$, respectively.	33
664	Fig. 2.	A one-dimensional schematic showing the relationship between the basis functions, the quadrature nodes and the proposed physics grid, over the coarse of a time-step. The filled circles are the GLL quadrature points in each element, which are connected by a Lagrange polynomials basis (curves). (a) Smooth initial condition are (b) advanced by the dynamics one Runge-Kutta step (blue), and (c) shows the solution after applying the DSS operator. Applying (d) grid-scale forcing to an element boundary node, (e) the basis representation is clearly C^0 at the element boundary. In contrast, (d) applying grid-scale forcing to an interior node (e) results in a smooth, C^∞ continuous field. (f),(i) Vertical bars pertain to the values on the physics grid, found through integrating the basis functions over the control volumes.	34
673	Fig. 3.	Probability density distribution of instantaneous upward ω in a pair of aqua-planet simulations using CAM4 physics. Figure is constructed from one year of six hourly data, at all vertical levels. (a) $ne30np4$ configuration conditionally sampled for interior, edge and corner node control volumes, and similarly (b) for the $ne30pg3$ configuration. The curves in (b) are overlaid in (a) in grey, and similarly the curves in (a) are overlaid in (b). Note the consistently larger magnitude ω for boundary nodes compared with interior nodes in (a), and that the bias is substantially reduced through mapping to a quasi-equal area physics grid.	35
680	Fig. 4.	An example of control volumes constructed around GLL quadrature points ($ne4np4$) so that the spherical area of the control volumes exactly match the quadrature weight multiplied by the metric factor.	36
683	Fig. 5.	A schematic illustration of an element, indicating the relationship between (left) the dynamical core grid, and (right) the proposed quasi-equal area physics grid. The physics grid contains $pg \times pg = 3 \times 3$ grid cells in each element.	37
686	Fig. 6.	L_2 difference norms of the surface pressure field, p_s , in the moist baroclinic wave simulations. L_2 values lying within the yellow region fall below the estimate of the uncertainty in the reference solution (black curve), computed as the difference norm between two approximately 0.25° resolution versions of CAM, the spectral-element and finite-volume (CAM-FV) dynamical cores.	38
691	Fig. 7.	Results of the terminator “toy”-chemistry test. Snapshot of the total column integrated, weighted sum of the species, $\langle Cl_y \rangle = \langle Cl \rangle + \langle 2Cl_2 \rangle$, in kg/kg, at day 15 of the moist baroclinic wave test. (Top) CAM-SE, (Bottom) CAM-SE-CSLAM.	39
694	Fig. 8.	Climatological zonal-mean total precipitation rate in the aqua-planets, computed from a pair of year long simulations.	40
696	Fig. 9.	Mean (left) and variance (right) of the low level temperature tendencies from the physical parameterizations on the GLL grid, with the $ne30np4$ configuration, (top row) and $ne30pg3$ configuration (bottom row), in a pair of year-long aqua-planet simulations. Grid imprint-	

699 ing is observed along the element boundaries in *ne30np4*, but is absent from the *ne30pg3*
700 simulation.

41

701 **Fig. 10.** Mean ω at two model levels in the middle troposphere, in a Held-Suarez configuration
702 outfitted with real world topography. (Left) CAM-SE state on the GLL grid, *ne30np4*,
703 (Middle) CAM-SE-CSLAM state on the physics grid, *ne30pg3* and (Right) their differences
704 computed through bi-linear interpolation to a common latitude-longitude grid. The ω fields
705 are computed from a 1200 day Held-Suarez simulation. The data are contoured according
706 to a ‘cell fill’ approach, in which the coupler grids (e.g, Figure 4) are used to delineate the
707 vertices of the control volumes.

42

708 **Fig. 11.** Climatological total precipitation rate (in mm/day) computed from the final 19 years of a
709 pair of 20 year long AMIP type simulations. (Left) CAM-SE, (middle) CAM-SE-CSLAM
710 and (Right) their differences.

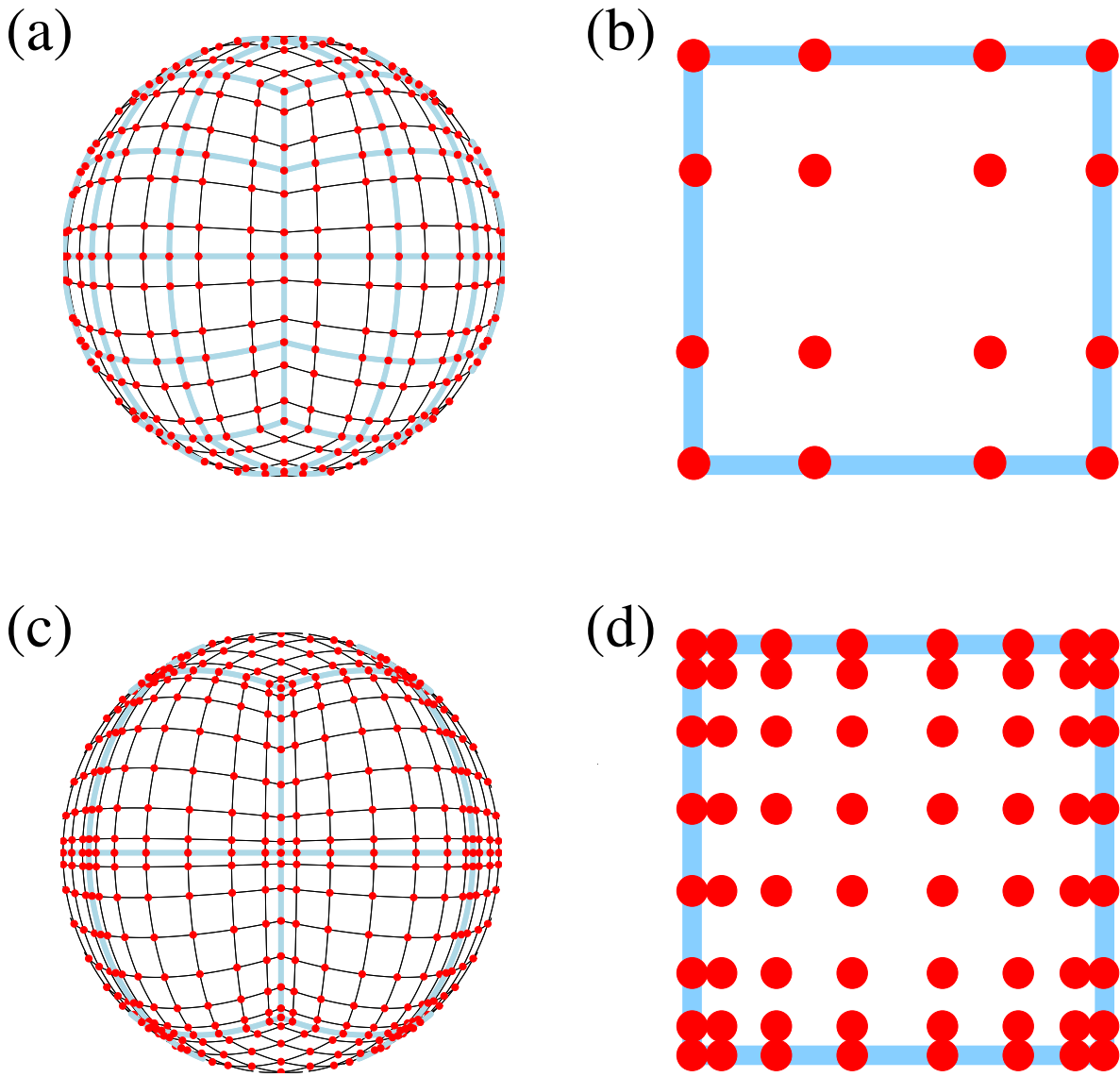
43

711 **Fig. 12.** Climatological total precipitation rate computed from the final 19 years of a suite of 20
712 year long AMIP simulations, using CAM-SE (*ne30np4*), CAM-SE-CSLAM (*ne30pg3*) and
713 CAM-FV (*f09*). The top plot is an observational product, the gridded GPCP climatological
714 precipitation dataset.

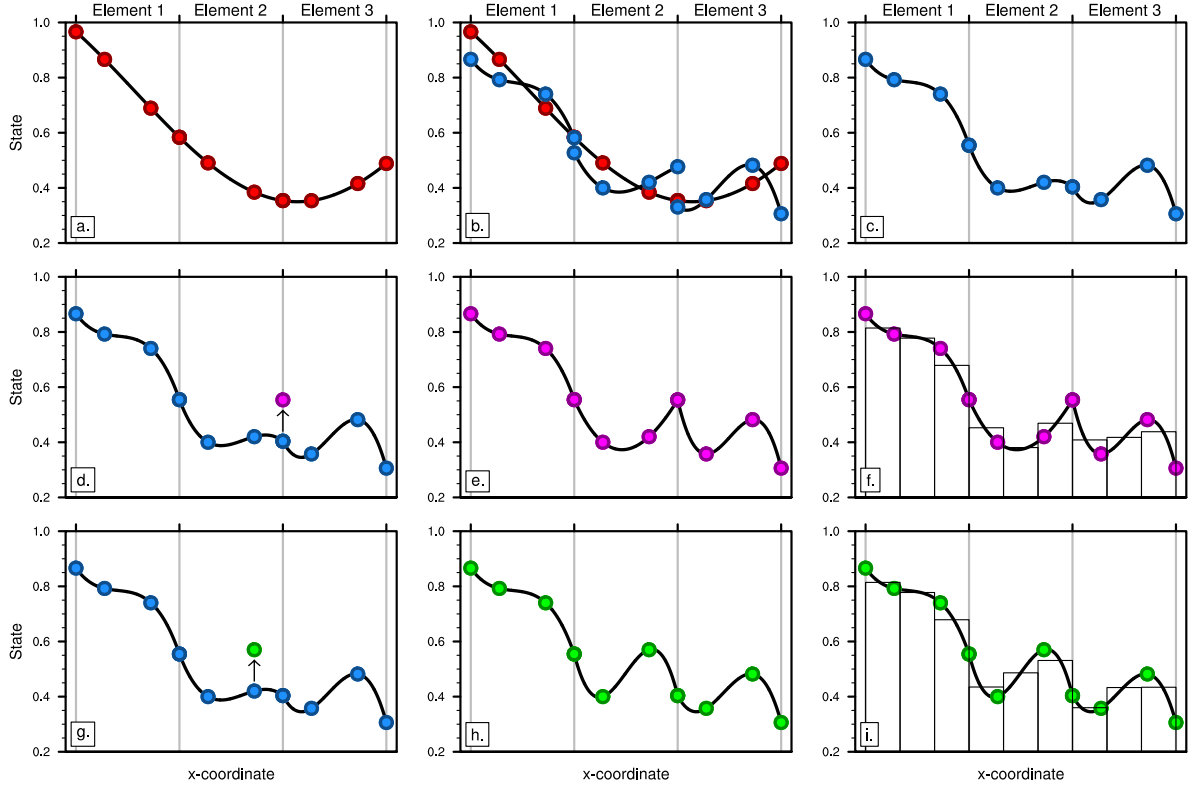
44

715 **Fig. 13.** Schematic of the coordinate system in which the dimensionally split cubic Lagrange in-
716 terpolation is computed. The physics grid centers are marked with asterisks and the GLL
717 points, we are interpolating to, with solid filled circles. The element in which the GLL
718 points are located is bounded by thick black lines and located in the lower left corner of a
719 panel. The stippled lines mark the boundaries of the remaining elements. For simplicity we
720 are using the normalized coordinate centered at the element on which the GLL points we
721 are interpolating to are located. Note that the coordinates for points on neighboring panels
722 (using a different local coordinate system) must be transformed to the coordinate system of
723 the element in question.

45



724 FIG. 1. Example of CAM-SE GLL quadrature grids, marked with red filled circles, (a & c) on the cubed-
 725 sphere and (b & d) in an element. (a)-(b) and (c)-(d) use 4×4 ($np = 4$) and 8×8 ($np = 8$) GLL quadrature
 726 points in each element, respectively. (a) and (c) have the same average grid-spacing at the Equator (7.5°) which is
 727 obtained by using (a) 4×4 ($ne = 4$) and (b) 2×2 ($ne = 2$) elements on each cubed-sphere face/panel, respectively.
 728 The element boundaries are marked with thick light blue lines. The grid configurations shown on (a) and (c) are
 729 referred to as $ne4np4$ and $ne2np8$, respectively.



730 FIG. 2. A one-dimensional schematic showing the relationship between the basis functions, the quadrature
 731 nodes and the proposed physics grid, over the coarse of a time-step. The filled circles are the GLL quadrature
 732 points in each element, which are connected by a Lagrange polynomials basis (curves). (a) Smooth initial con-
 733 dition are (b) advanced by the dynamics one Runge-Kutta step (blue), and (c) shows the solution after applying
 734 the DSS operator. Applying (d) grid-scale forcing to an element boundary node, (e) the basis representation is
 735 clearly C^0 at the element boundary. In contrast, (d) applying grid-scale forcing to an interior node (e) results
 736 in a smooth, C^∞ continuous field. (f),(i) Vertical bars pertain to the values on the physics grid, found through
 737 integrating the basis functions over the control volumes.

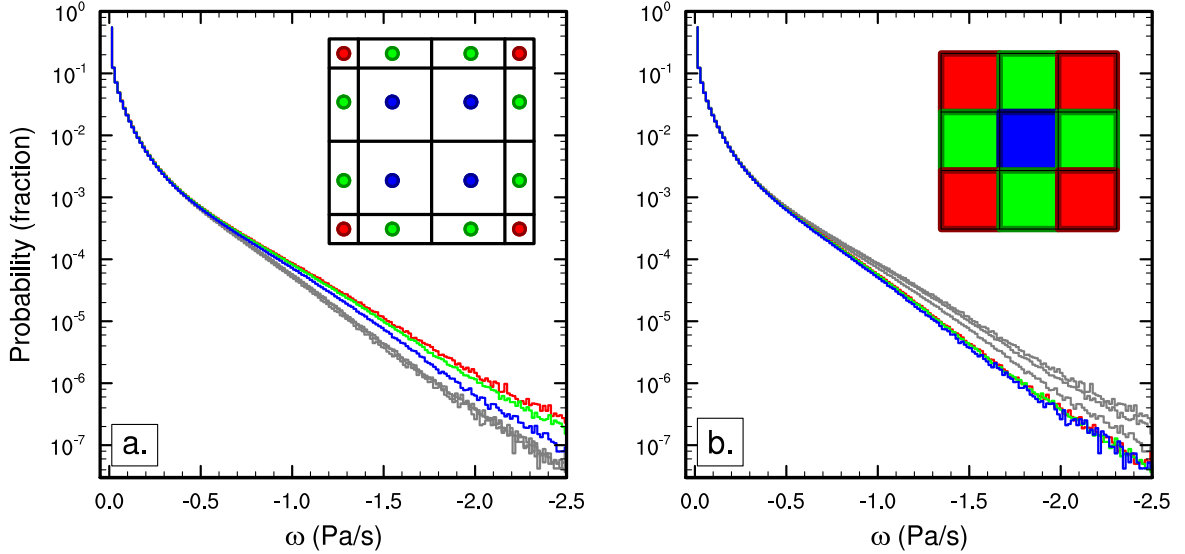
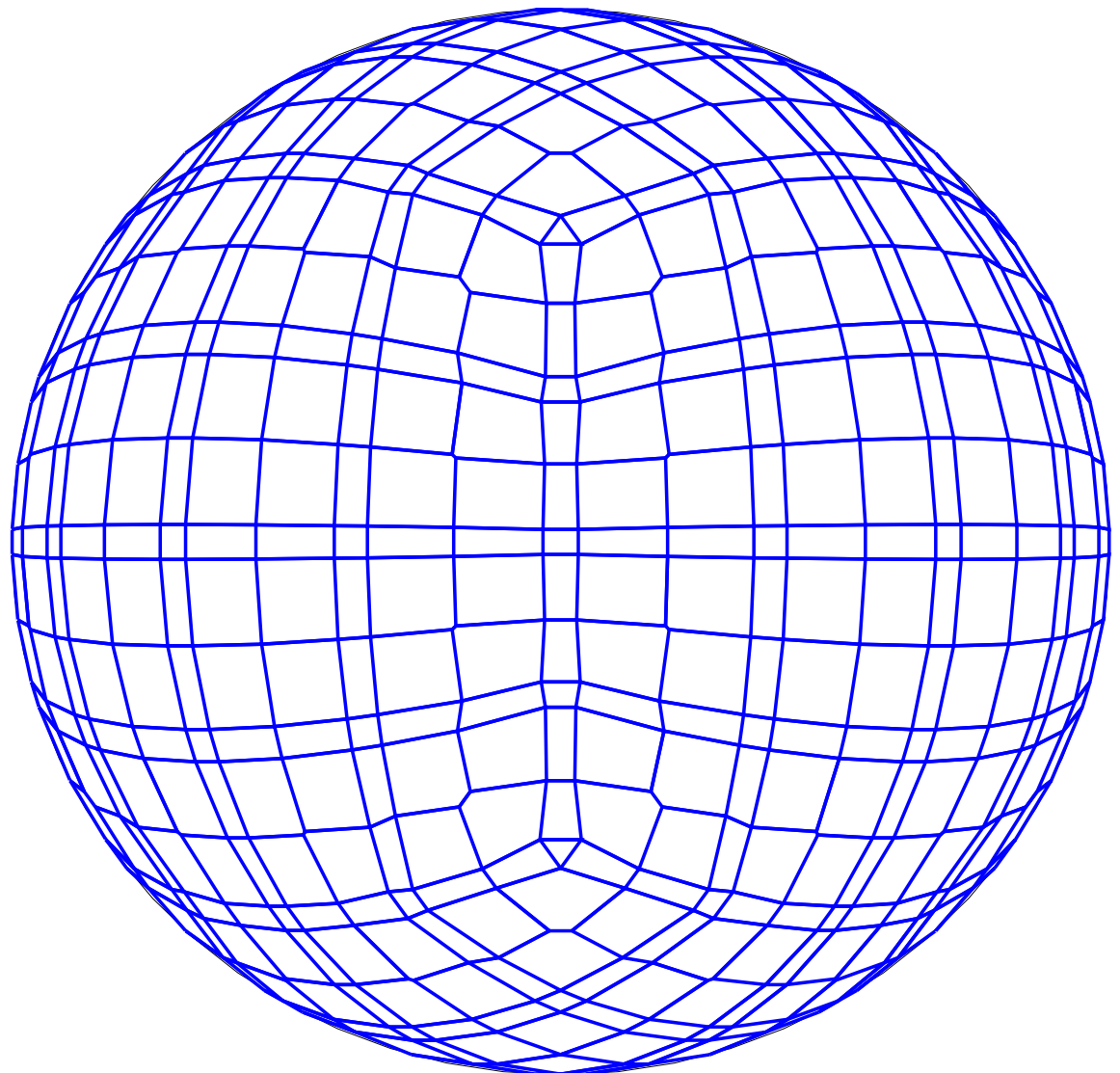
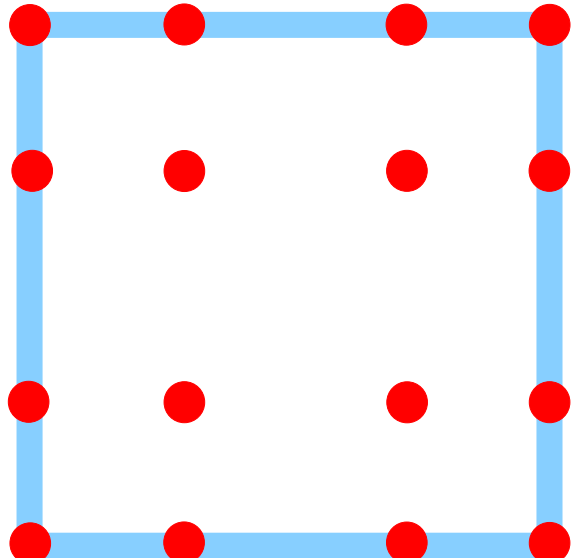


FIG. 3. Probability density distribution of instantaneous upward ω in a pair of aqua-planet simulations using CAM4 physics. Figure is constructed from one year of six hourly data, at all vertical levels. (a) *ne30np4* configuration conditionally sampled for interior, edge and corner node control volumes, and similarly (b) for the *ne30pg3* configuration. The curves in (b) are overlain in (a) in grey, and similarly the curves in (a) are overlain in (b). Note the consistently larger magnitude ω for boundary nodes compared with interior nodes in (a), and that the bias is substantially reduced through mapping to a quasi-equal area physics grid.

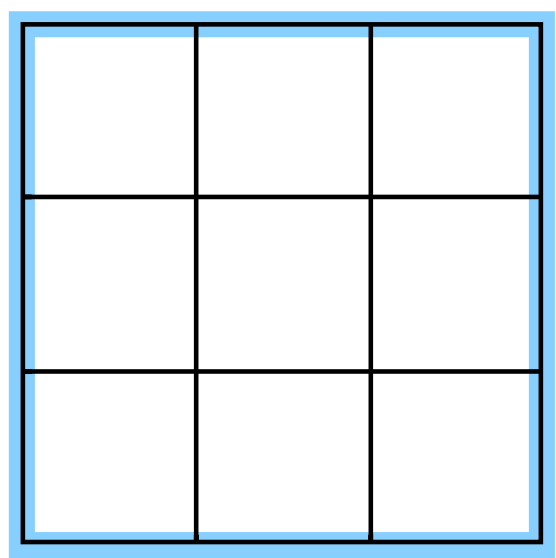


744 FIG. 4. An example of control volumes constructed around GLL quadrature points ($ne4np4$) so that the
745 spherical area of the control volumes exactly match the quadrature weight multiplied by the metric factor.

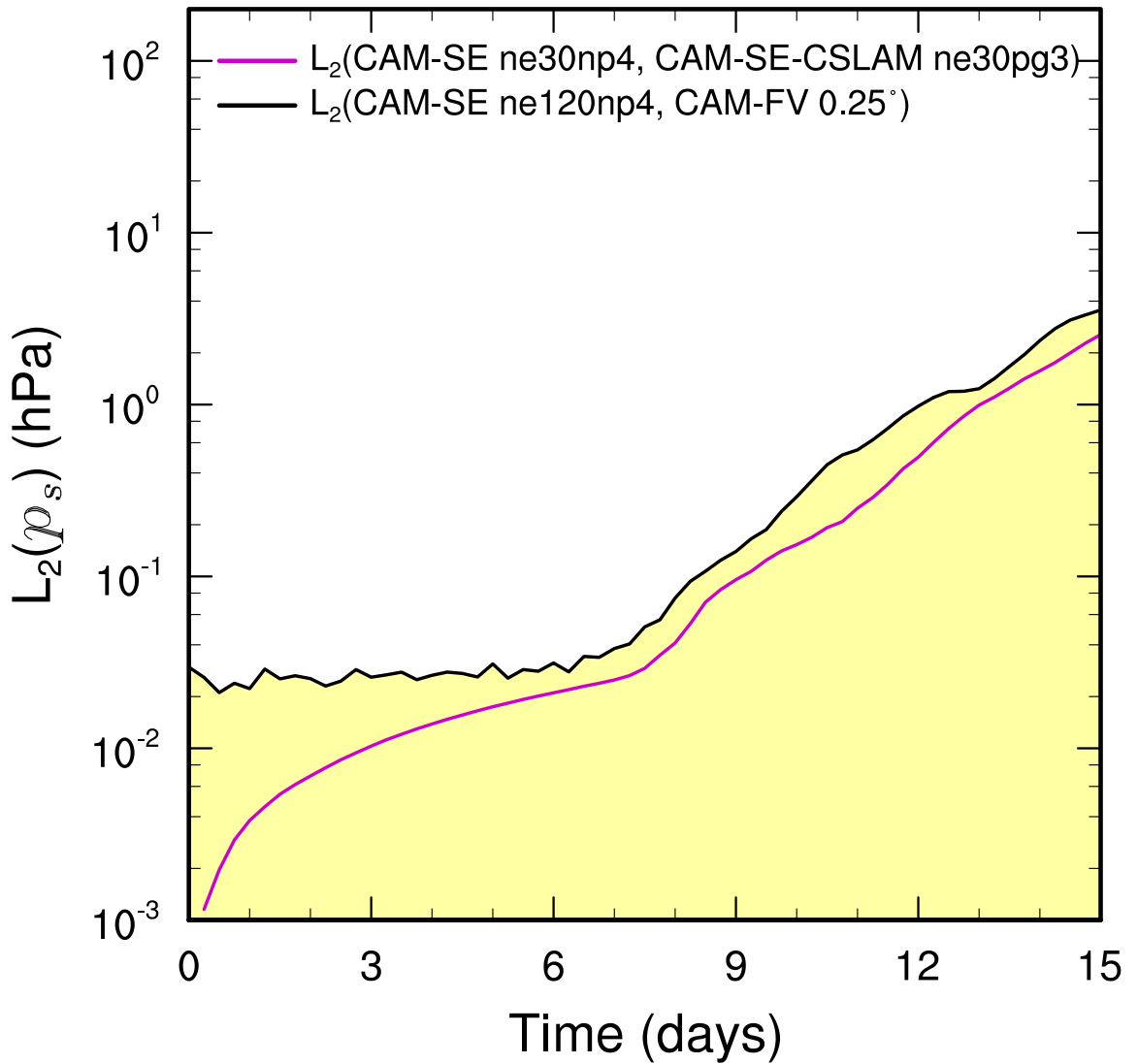
$$np = 4$$



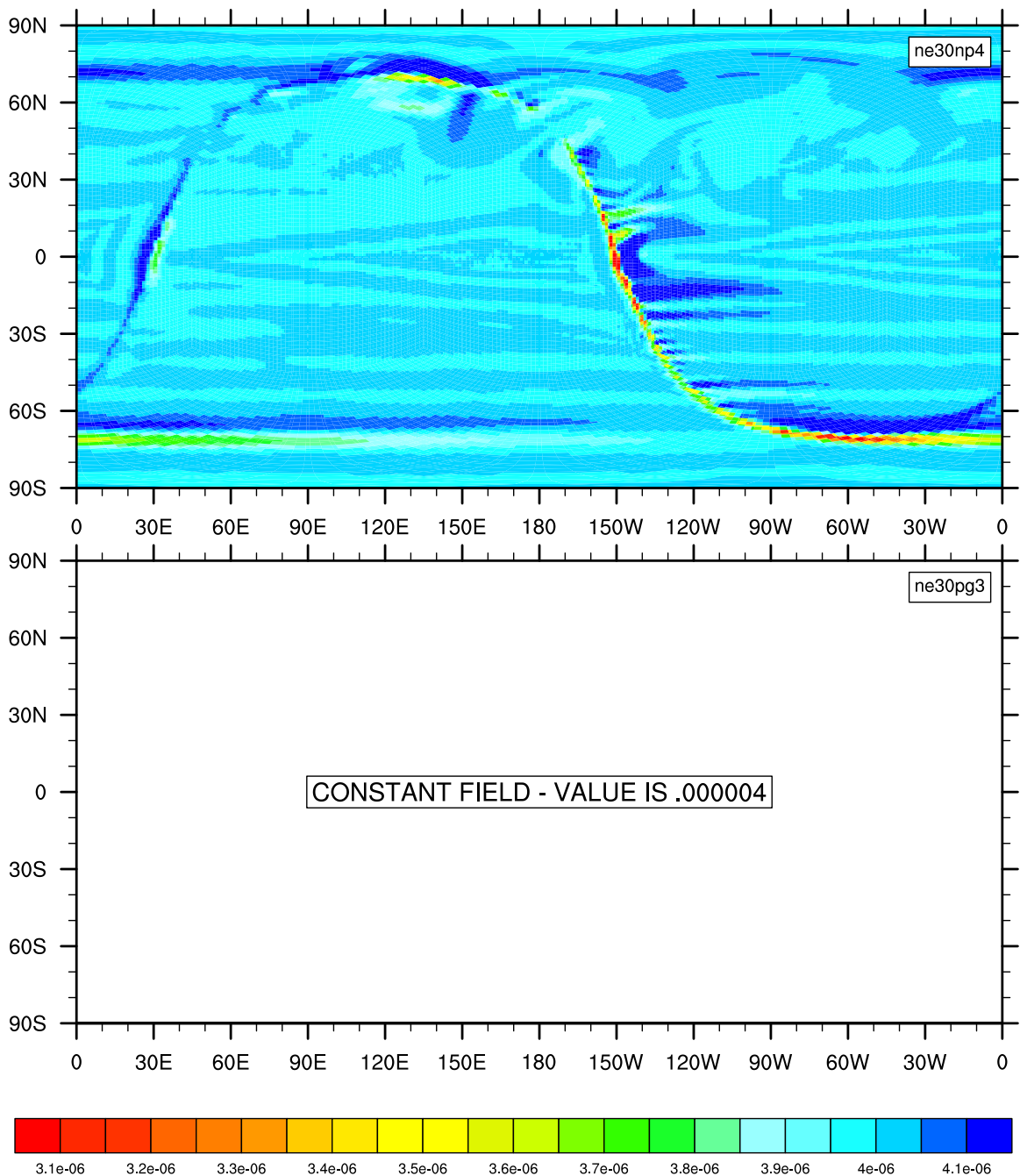
$$pg = 3$$



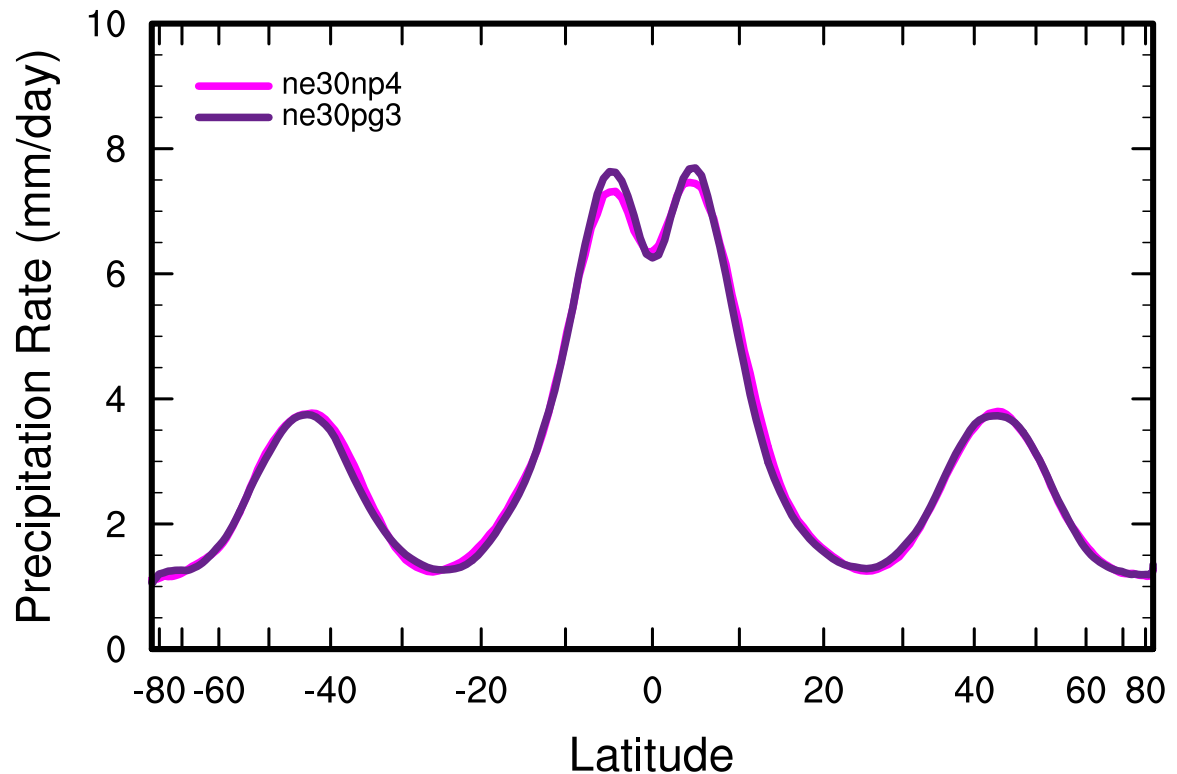
746 FIG. 5. A schematic illustration of an element, indicating the relationship between (left) the dynamical core
747 grid, and (right) the proposed quasi-equal area physics grid. The physics grid contains $pg \times pg = 3 \times 3$ grid cells
748 in each element.



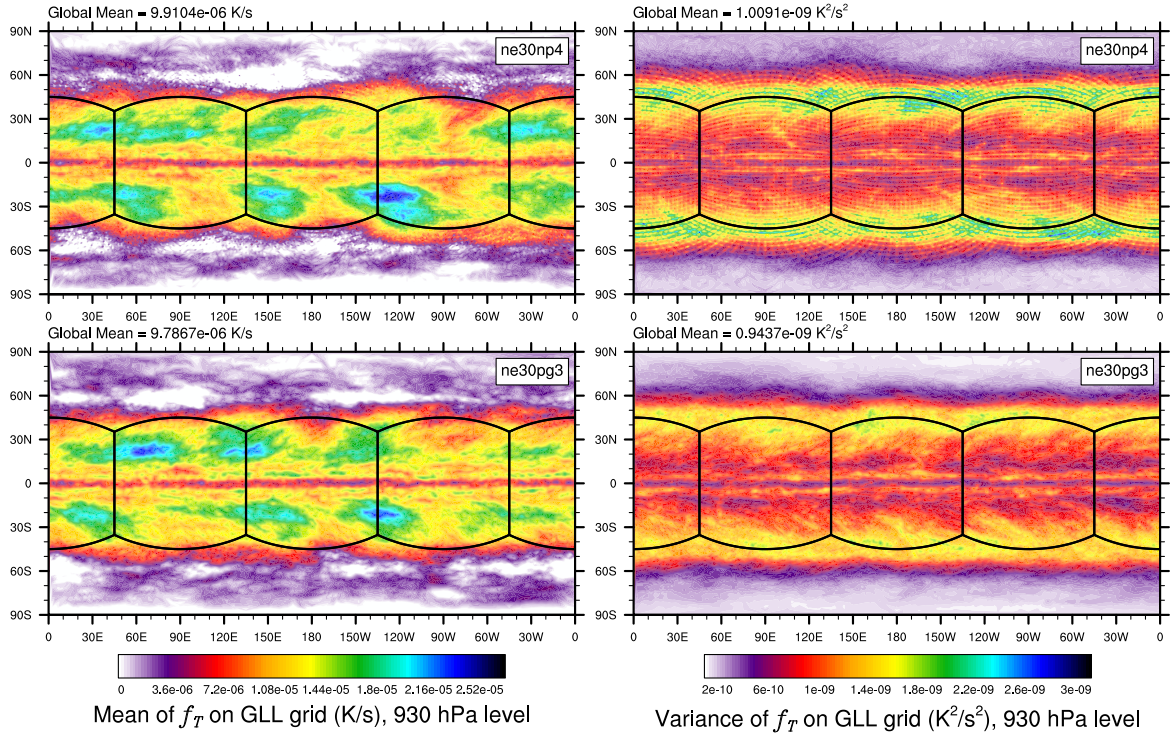
749 FIG. 6. L_2 difference norms of the surface pressure field, p_s , in the moist baroclinic wave simulations. L_2
 750 values lying within the yellow region fall below the estimate of the uncertainty in the reference solution (black
 751 curve), computed as the difference norm between two approximately 0.25° resolution versions of CAM, the
 752 spectral-element and finite-volume (CAM-FV) dynamical cores.



753 FIG. 7. Results of the terminator “toy”-chemistry test. Snapshot of the total column integrated, weighted sum
 754 of the species, $\langle Cl_y \rangle = \langle Cl \rangle + \langle 2Cl_2 \rangle$, in kg/kg, at day 15 of the moist baroclinic wave test. (Top) CAM-SE,
 755 (Bottom) CAM-SE-CSLAM.



756 FIG. 8. Climatological zonal-mean total precipitation rate in the aqua-planets, computed from a pair of year
757 long simulations.



758 FIG. 9. Mean (left) and variance (right) of the low level temperature tendencies from the physical parameter-
 759 izations on the GLL grid, with the *ne30np4* configuration, (top row) and *ne30pg3* configuration (bottom row),
 760 in a pair of year-long aqua-planet simulations. Grid imprinting is observed along the element boundaries in
 761 *ne30np4*, but is absent from the *ne30pg3* simulation.

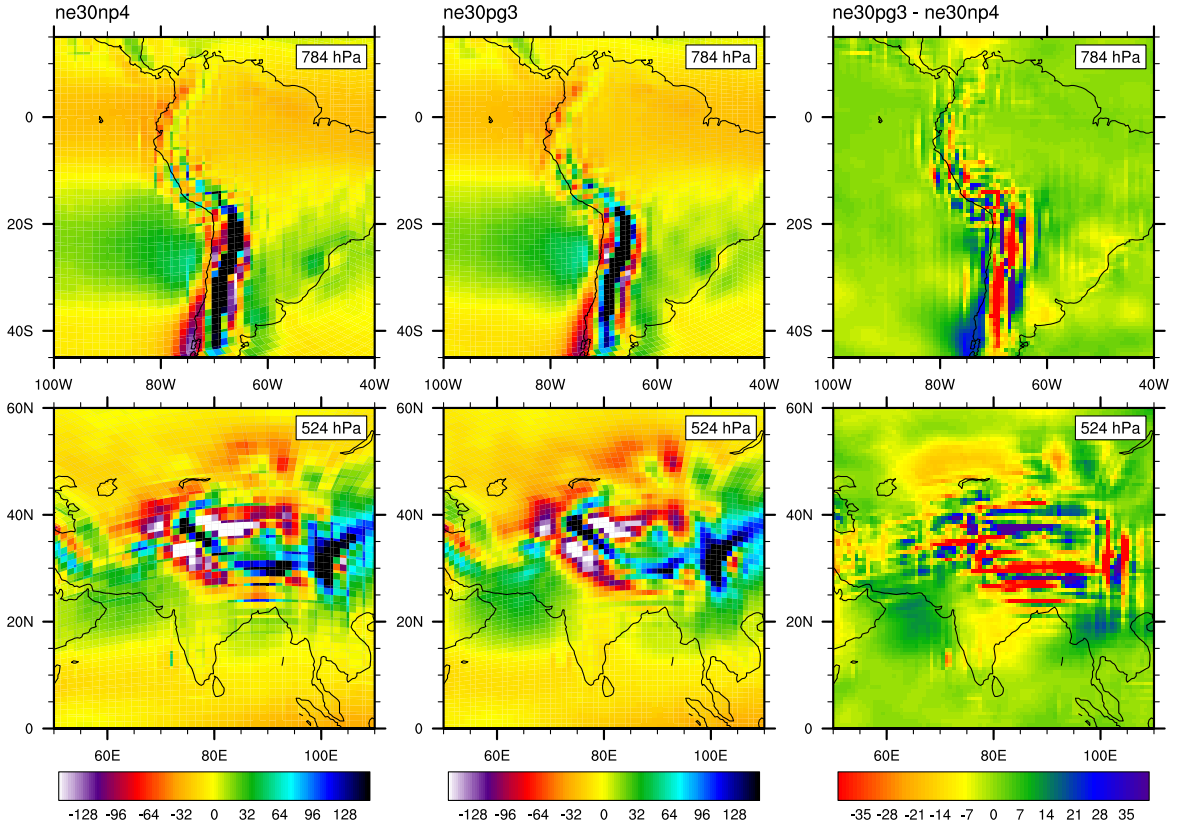
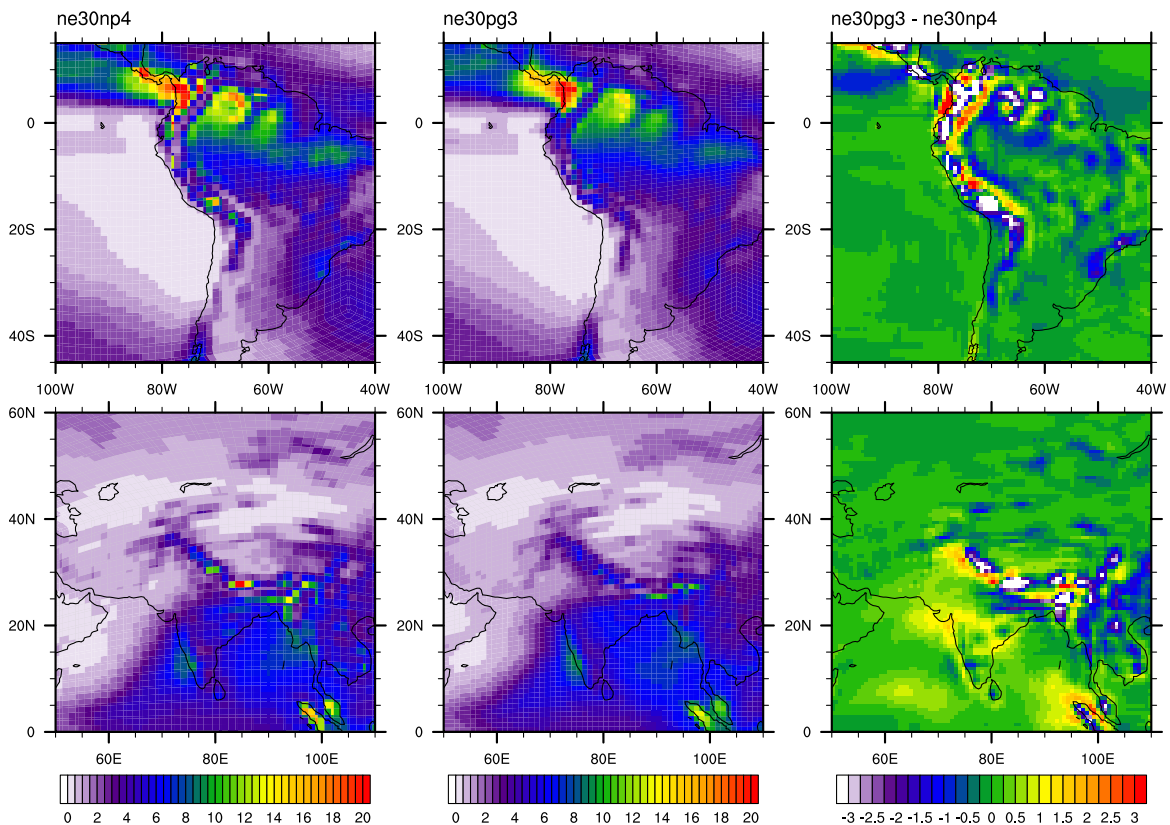
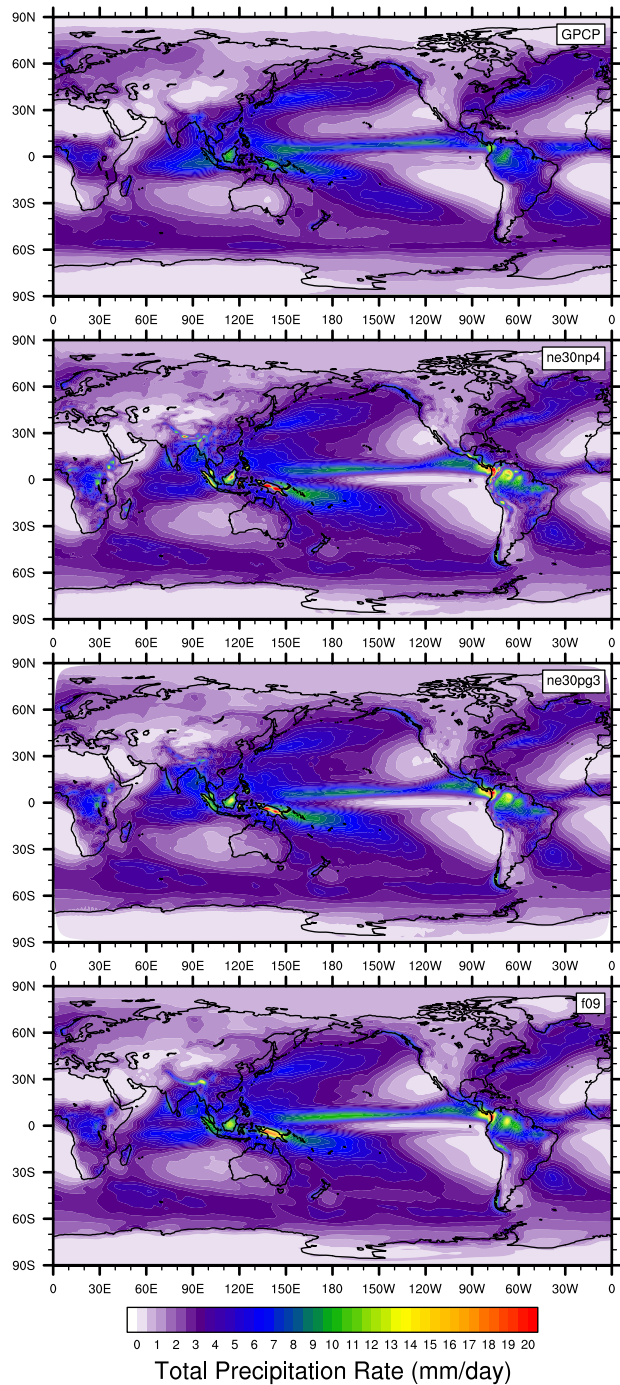


FIG. 10. Mean ω at two model levels in the middle troposphere, in a Held-Suarez configuration outfitted with real world topography. (Left) CAM-SE state on the GLL grid, *ne30np4*, (Middle) CAM-SE-CSLAM state on the physics grid, *ne30pg3* and (Right) their differences computed through bi-linear interpolation to a common latitude-longitude grid. The ω fields are computed from a 1200 day Held-Suarez simulation. The data are contoured according to a ‘cell fill’ approach, in which the coupler grids (e.g, Figure 4) are used to delineate the vertices of the control volumes.



768 FIG. 11. Climatological total precipitation rate (in mm/day) computed from the final 19 years of a pair of 20
 769 year long AMIP type simulations. (Left) CAM-SE, (middle) CAM-SE-CSLAM and (Right) their differences.



770 FIG. 12. Climatological total precipitation rate computed from the final 19 years of a suite of 20 year long
 771 AMIP simulations, using CAM-SE (ne30np4), CAM-SE-CSLAM (ne30pg3) and CAM-FV (f09). The top plot
 772 is an observational product, the gridded GPCP climatological precipitation dataset.

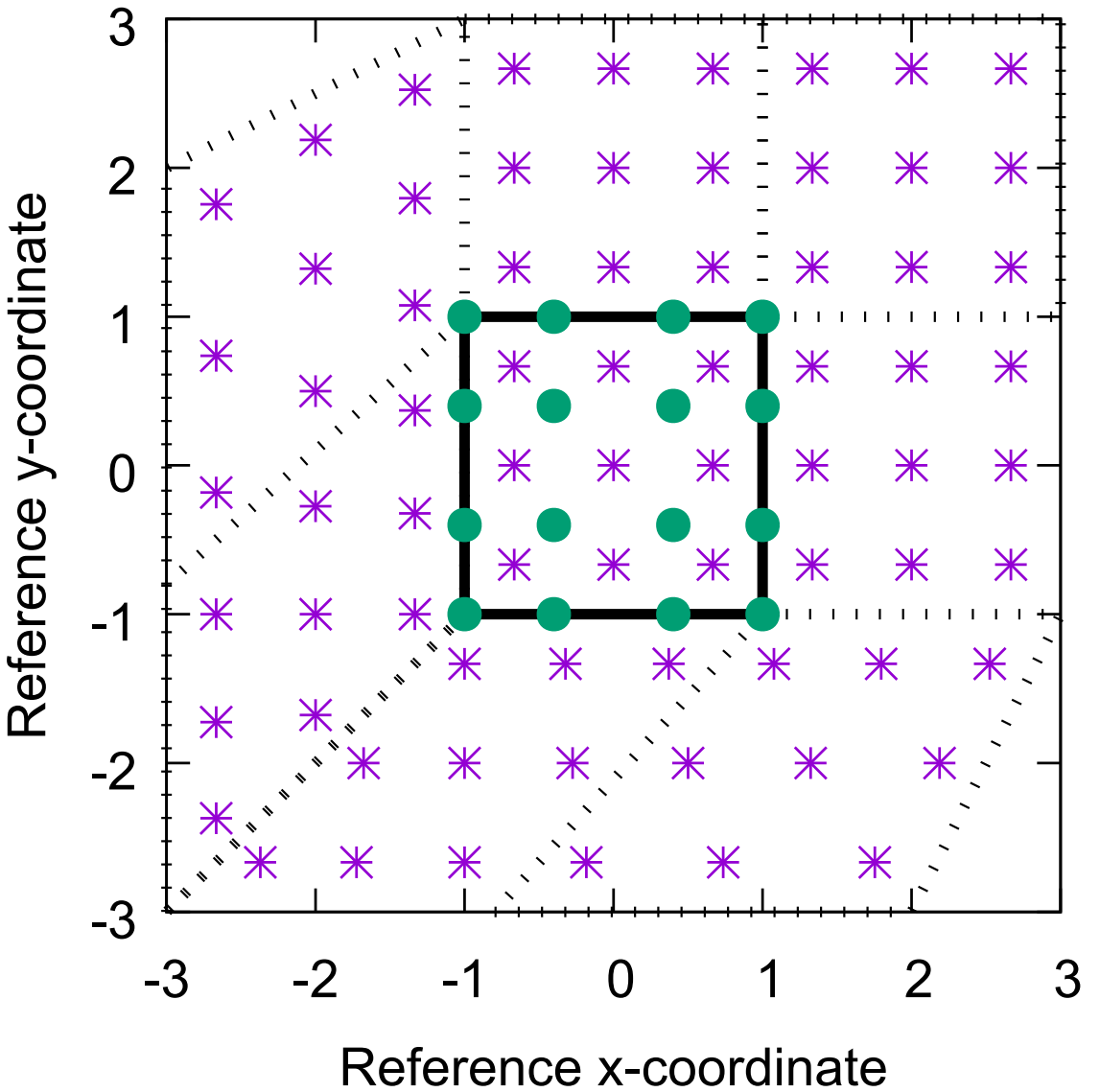


FIG. 13. Schematic of the coordinate system in which the dimensionally split cubic Lagrange interpolation
 is computed. The physics grid centers are marked with asterisks and the GLL points, we are interpolating to,
 with solid filled circles. The element in which the GLL points are located is bounded by thick black lines and
 located in the lower left corner of a panel. The stippled lines mark the boundaries of the remaining elements.
 For simplicity we are using the normalized coordinate centered at the element on which the GLL points we are
 interpolating to are located. Note that the coordinates for points on neighboring panels (using a different local
 coordinate system) must be transformed to the coordinate system of the element in question.